Article:
Le Guillou, C, Dohmen, R, Rogalla, D et al. (3 more authors) (2015) New experimental approach to study aqueous alteration of amorphous silicates at low reaction rates. Chemical Geology, 412. pp. 179-192. ISSN 0009-2541

https://doi.org/10.1016/j.chemgeo.2015.06.027

New experimental approach to study aqueous alteration of amorphous silicates at low reaction rates.

Corentin Le Guillou[1*], Ralf Dohmen[1], Detlef Rogalla[2], Thomas Müller[1,3], Christian Vollmer[4] and Hans-Werner Becker[2]

[1]Institut für Geologie, Mineralogie und Geophysik, Ruhr-Universität Bochum, Bochum, Germany. [*]corentin.san@gmail.com
[2]RUBION - Zentrale Einrichtung für Ionenstrahlen und Radionuklide, Ruhr-Universität Bochum, DE-44780 Bochum, Germany
[3]Institute of Geophysics and Tectonics, School of Earth and Environmental Sciences, University of Leeds, Leeds LS2 9JT
[4]Institut für Mineralogie, Westfälische Wilhelms-Universität Münster, Corrensstr. 24, D-48149 Münster, Germany.

Abstract

Understanding the kinetics of silicate alteration in aqueous media is central to the study of oceanic hydrothermal systems, nuclear glass durability or carbonaceous asteroids from which chondrites are coming. We present a new experimental approach in combination with an integrated analytical protocol designed to study alteration processes at low temperatures (< 200°C) and slow reaction rates. We used pulsed laser deposition (PLD) to produce micrometer thick films of amorphous silicate of controlled chemical composition. After reacting with water in sealed capsules, the films consist of a succession of compositionally different layers. The initial planar geometry of the film allows a complete characterization of the transformed materials at the nanometer scale. By combining Rutherford back-scattering (RBS), nuclear reaction analysis (NRA), transmission electron microscopy (TEM) and scanning transmission X-ray microscopy (STXM), it is possible to constrain the propagation rate of the reaction fronts, the thicknesses of individual layers, spatial variations in composition, the nature of the interface between the layers, the iron redox state, the water content along depth profiles, as well as the porosity and the density.

We investigated the serpentinization of amorphous silicate films with stoichiometry close to olivine (~ $Fe_{1.1}Mg_{0.9}SiO_{4.15}H_{0.3}$) at 90°C (2 weeks) and 200°C (2 hours). In both cases, ~ 500 nm of altered material are formed. At the reaction front, a hydrated, amorphous and oxidized Fe-rich layer forms. At the interface with the fluid, a more Mg-rich layer develops. The system evolves towards a biphasic assemblage of Fe-serpentine and Mg-saponite composition. Both

layers remain amorphous. It is shown that water propagation is coupled to hydrolysis, iron oxidation ($Fe^{3+}/\sum Fe$ ratio > 50%) and H_2 formation, whose quantifications are crucial to understand terrestrial serpentinization processes. Interfacial precipitation-dissolution seems to be the rate controlling mechanisms. In addition, we investigated a crystallized film reacted at 190°C (2 hours), which transformation rate is ten times slower than that of the amorphous silicate but is nevertheless readily observable. This approach can be used to understand alteration in terrestrial and extraterrestrial samples. In particular, we reproduced several features observed in carbonaceous chondrites (amorphous and oxidized hydrated silicates) and show that, at 90°C, alteration may be faster than usually considered. It should allow us in the future to constrain the temperatures and timescales of alteration in chondrites.

Keywords

Aqueous alteration; chondrites; amorphous silicate; serpentinization; nano-analysis; experiments; reaction rates; mineral-water interaction

1. Introduction

Alteration of silicates at low temperatures is a common process in geosciences and cosmochemistry. It occurs in many different environments such as continental surfaces (Hellmann et al., 2003; Godderis et al., 2010), oceanic floor (Berger et al., 1987; Crovisier et al., 2003; Schramm et al., 2005; Benzerara et al., 2007; Klein et al., 2009; Andreani et al., 2013), or meteorites and asteroids (Tomeoka and Buseck, 1988; Brearley, 2006 and references therein; Morlok and Libourel, 2013). In addition, it is also a major topic of discussion in material sciences for purposes like alteration of glasses used for nuclear waste confinement (Frugier et al., 2008; Valle et al, 2010), alteration of archeological glasses (Dohmen et al., 2013), or silicate carbonation for CO_2 sequestration purposes (Knauss et al., 2005; Daval et al., 2009; Hövelmann et al., 2012). However, our understanding of the kinetic laws controlling such processes is limited. This is mainly due to difficulties in constraining the reaction mechanisms, especially at the relevant low temperature ranges (< 100 - 150°C) and because the physico-chemical models extrapolating the experimental results to natural environments are still debated (Hellmann et al., 2012; Daval et al., 2013; Malvoisin et al., 2014).

Our long term goal is to constrain the temperature and timescales of hydrothermalism in asteroids, from which chondrites are formed. These meteorites carry a record of the earliest solar system processes, including water-silicate interactions. In particular, amorphous silicates are observed in the interstellar medium and protoplanetary disks (Dorschner and Henning, 1995; Kemper et al., 2004) and are also observed in primitive chondrites (Brearley, 1993). At the time of the formation of the solar system, asteroids have accreted water as ice, together with iron-rich amorphous silicates (Le Guillou and Brearley, 2014). The latter were likely condensed from the

gas phase (Nuth et al., 2005; Pontopiddan and Brearley, 2010). Water and silicate have then reacted and the alteration products are now found in CI, CM or CR carbonaceous chondrites (Zolensky et al., 1989; Rubin et al., 2007; Chizmadia and Brearley, 2008; Abreu and Brearley, 2010; Zolotov, 2012). Alteration formed diverse minerals including hydrated amorphous silicates, serpentine-type phases (Mg-chrysotile or oxidized Fe-cronstedtite), and a suite of minor phases such as iron oxides and hydroxides, sulfides and carbonates (Tomeoka and Buseck, 1988; Brearley, 1993, 2006; Lauretta et al., 2000; Rubin et al., 2007; Le Guillou et al., 2014, 2015). In particular, a hydrated amorphous iron-rich silicate and serpentine are found in all groups of carbonaceous chondrites. Unraveling their formation and hydration conditions is a key to understand the origin of matrices and their hydrothermalism history (Abreu and Brearley, 2010; Le Guillou and Brearley, 2014; Le Guillou et al., 2015). To that end, it is crucial to quantitatively constrain the kinetics and the operating mechanisms of amorphous silicate alteration. A few studies have experimentally investigated alteration in chondrites (Jones and Brearley, 2006; Ohnishi et al., 2007), but they only addressed the alteration of crystalline material at temperatures above 150 °C. However, experiments focusing on the specificity of amorphous silicate and of low temperatures processes are required. Ultimately, this will enable estimating the timescales of hydrothermalism, and how water was consumed and/or degassed in asteroids.

Serpentinization reactions are very sluggish at temperatures below 200 °C, and are therefore not trivial to study within laboratory timescales, as the reacted volumes are typically limited (Malvoisin et al., 2012a,b). In fluid-mediated reactions (opposed to a solid-state transformation), dissolution is often a prerequisite to the formation of secondary phases, and kinetic competition occurs between various mechanisms such as dissolution, precipitation, hydrolysis and oxidation reactions, as well as water and cations transport through the porosity of the precipitated materials (O'Neil and Taylor, 1967; Berger et al., 1987; Banfield et al., 1995; Crovisier et al., 2003; Hellmann et al., 2003; Frugier et al., 2008; Daval et al., 2009, 2013; Mueller et al., 2010; Valle et al., 2010; Ruiz-Agudo et al., 2014).

Different types of experimental strategies have been used to study silicate alteration. Olivine serpentinization is often studied in closed system setups, using powders as starting materials (Marcaillou et al., 2011; Malvoisin et al., 2012a,b). The solid phases are then characterized by SEM, X-ray diffraction Mossbauer spectroscopy, XANES or magnetic monitoring, among other (Marcaillou et al., 2011; Malvoisin et al., 2012). One difficulty with powder experiments is that the grain size distribution changes during progressive alteration.Thus the specific rate of the chemical reactions requires integrating the evolution of the surface to volume ratio over time, which is not straightforward. Another issue arises from the fact that crystalline olivine is not reactive within laboratory timescales at temperatures below 200 °C, and that few data are available within the temperature range relevant for chondrites. Studies on glass alteration performed at lower temperatures are generally conducted in semi-open systems (fresh H_2O continuously brought to the reaction cell at a slow rate) which consequently leads to a higher alteration rate, but do not adequately simulate chondritic environments (i.e. closed system and

low fluid to rock ratio). Most studies use fluid analysis as the main analysis tool. It allows to determine the relative rates of dissolution of different elements, but it does not contain much information about the temporal evolution of the solid phase, which are rarely studied (Valle et al., 2010). In chondrites, only the solids are available and their study is required to understand the reaction mechanisms.

In order to investigate amorphous silicates alteration at low temperature, i.e. to precisely study their reaction mechanisms and kinetics, we designed a novel experimental protocol. Specific requirements have to be met for the study of chondritic amorphous silicate: 1) synthesizing amorphous iron-rich precursors of micrometer dimension, 2) running the experiments in closed system, and 3) being able to characterize the solid products with nanometer scale resolution. We used the pulsed laser deposition (PLD) technique to synthesize a starting material of desired composition (Dohmen et al., 2002). A one micron thick amorphous layer is deposited from a plasma on a polished surface substrate. During the alteration process, successive layers of altered materials form progressively from the surface down towards the depth of the film. The film can also be pre-annealed at high temperature prior the alteration experiment in order to obtain a fine-grained, polycrystalline film, allowing for direct comparison of reaction rates of amorphous and crystallized material of similar composition. The ideal, flat geometry allows combining complementary analytical techniques to fully characterize the products at the nanometer scale. The surface to volume ratio is also easily determined. We combined, in an integrated manner, Rutherford back-scattering (RBS), nuclear reaction analysis (NRA), focused ion beam (FIB) coupled with transmission electron microscopy (TEM) and scanning-transmission X-ray microscopy (STXM) in order to: study the reaction front advancement, determine the composition and physical properties (density, porosity) of each layer, characterize each layer boundaries, measuring the water content of different layers with tens of nanometer resolution, spatially determine the redox state of iron to assess the role of redox reactions, and establish a mass budget to discuss the transport processes within the materials.

In this paper, we describe our experimental setup, and discuss how to efficiently combine and optimize the outcome of each analytical technique. We then present examples of experiments comparing initially crystalline and amorphous materials to illustrate how these information can be successfully used to constrain the mechanism and rates of reaction. Finally, this new combination of experimental and analytical protocol is used to discuss the conditions of hydrothermalism of chondritic materials.

2. Experiments and characterization methods

2.1. Experimental setup

2.1.1. Sample preparation: Pulsed laser deposition and annealing

Pulsed laser deposition is a method which allows synthesizing various types of material of controlled composition in their amorphous state. An Excimer laser is used to ablate a target of

known composition, which results in a plasma (Fig. 1). The latter condenses on a substrate. Different deposition rates can be achieved depending on the laser intensity (laser fluence, energy per surface area of the target), wavelength and the target composition, which are typically in the range of 1 to 10 nm per minute for most silicates (Dohmen et al., 2002).

In the present study, we use a 193 nm wavelength laser (power around 300 mJ per pulse, operating at 20 kV, 10 Hz). After passing through the optics, the beam is focused on a mm large area with a power of ~ 40-50 mJ/pulse (Watson and Dohmen, 2010). We used a synthetic polycrystalline target composed of fayalitic olivine (fayalite 50) and the plasma condenses under high vacuum (~ 10^{-5} Pa) on polished, 001 oriented 0.5 mm thick TiO_2 substrates (© Crystec), which were cut to cylinders with diameter of approximately 5 mm. TiO_2 has very low solubility and dissolution rates at the present experimental conditions and is thus considered to be inert. The substrate is first heated to about 400 °C in order to degas and to clean its surface before deposition. After cooling, 500 nm to 2 micrometer thick films were deposited in timescales of hours.

In order to compare the reactivity of amorphous and crystalline olivine, we annealed an amorphous film at 900 °C under controlled oxygen fugacity for several hours. The film recrystallized into an ultra-fine grained polycrystalline aggregate with ~ 100 nm-sized crystalline domains (Dohmen et al., 2002). Details on the characterization of the starting material are presented in section 3.

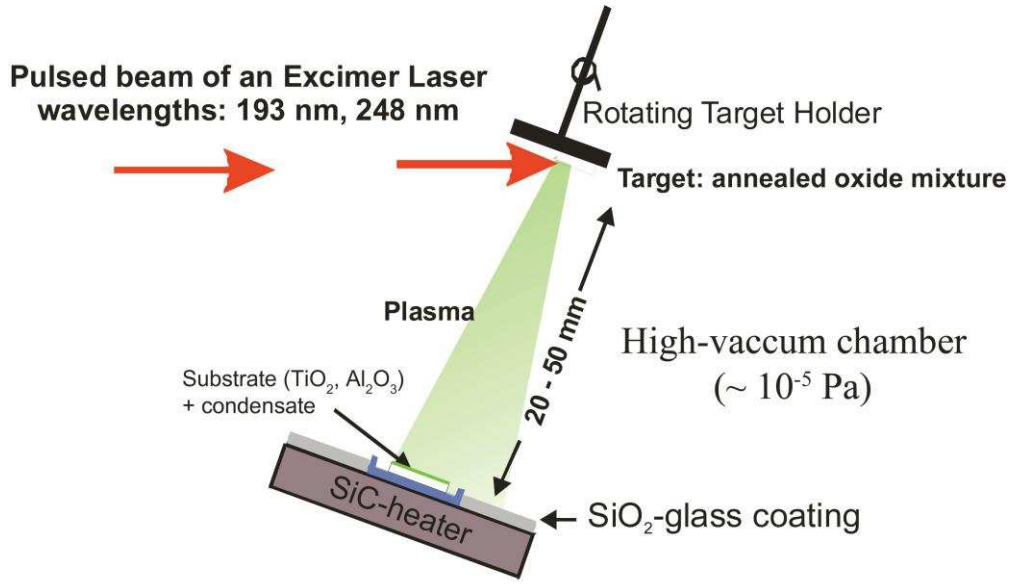

Fig. 1: Scheme of the pulsed laser deposition setup. The laser hits a synthetic olivine (Fayalite 50 composition). Under high vacuum, a plasma is created and condenses on the substrate (TiO_2 in this case). The effective deposition rate is around 500 nm/hour for this composition.

2.1.2. Hydrothermal experiments

The films deposited on the substrates are positioned at the bottom of a gold capsule (6 mm inner diameter), whose extremity has been first sealed and pressed at 30 $x10^5$ Pa to be flattened. Twenty-five microliters of water are then introduced at the bottom of the capsule within a glove box filled with N_2 (Fig. 2). The water pH is buffered by adding KOH at pH 9, close to the pH of chondritic fluids (Brearley et al., 2006; Zolotov et al., 2012). The capsule is then sealed with an electric arc. The capsule containing the sample is weighted before and after sealing to check for potential water loss and leakage of the capsule during the experiment. It is then placed in a Teflon bomb filled with water. Using this setup, samples can be heated to temperatures between 20 and 250 °C, at pressures between 1 and 3.5 $x10^5$ (see Table 1 for details). The presence of water inside and outside the capsule ensures a similar pressure in both reservoirs and therefore prevents water leaks which would be driven by pressure gradients. An amorphous film with a diameter of 5 mm and a thickness of 2 micrometers has a surface to volume ratio of 500 000 m^{-1} and a surface to fluid volume ratio of 950 m^{-1}. The corresponding water to rock mass ratio is therefore ~ 150.

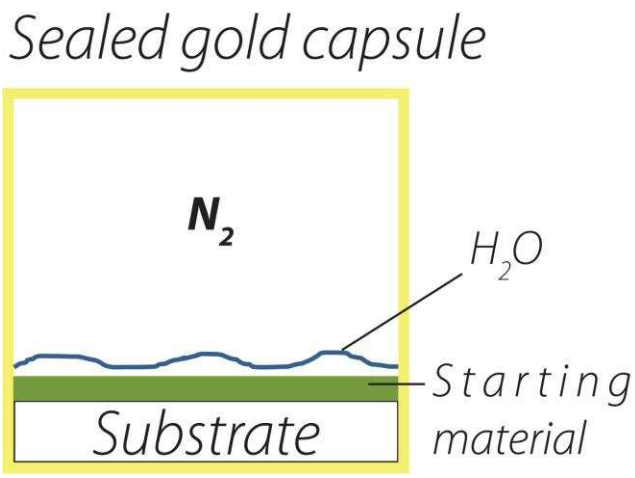

Fig. 2: Schematic drawing of the gold capsule containing the film deposited on the substrate at the bottom. The capsule diameter is 6 mm. The film thickness is between 500 nm and 3 micron depending on the experiments.

2.2. Characterization methods and measurement conditions

We combined a number of analytical techniques in order to obtain a full picture of the reacted solids. Each of the techniques described below allows to access a different property: scanning electron microscopy (SEM) images the surface of the film; Rutherford back scattering (RBS) measures a compositional depth profile of the major elements; nuclear reaction analysis (NRA) yields variations of the H concentration with depth; FIB/TEM constraints the composition and mineralogy of the reacted and unreacted layers at the nanometer scale; and scanning transmission

X-ray microscopy (STXM) is a synchrotron based spectromicroscopy method which allows determining the valency state of iron at the nanometer scale.

2.2.1. Scanning electron microscopy (SEM)

To document the surface of the reacted films, we used a Zeiss LEO 1530 Gemini FESEM equipped with an inlens detector, allowing a nanometer scale lateral resolution to be achieved.

2.2.2. Rutherford backscattering spectroscopy (RBS)

Rutherford backscattering spectroscopy (RBS) was carried out at the Dynamitron Tandem Accelerator facility of the Ruhr-University of Bochum. It is a depth resolved mass spectrometry technique of near surface layers. We used a single charged He beam (2 MeV with a beam intensity of 2 nA) of alpha particles in combination with a silicon particle detector at a backscattering angle of 160° and a solid angle of 1.9 msrad. The beam is collimated to a diameter of 0.5 mm. The spectra were analyzed using the software RBX (Kotai, 1994), which allows determining the stoichiometry of the different layers and the substrate as well as their thickness or densities (i.e., the density of a given layer can be determined if the thickness is known, and vice versa). The stoichiometry and thickness of the layers are adjusted to fit the observed spectra.

2.2.3. Nuclear reaction analysis (NRA)

NRA was been carried out with the ^{15}N beam of the Dynamitron Tandem of the University of Bochum (Traeger et al., 2011), providing a beam intensities of up to 300 nA (triply-charged ^{15}N beam corresponding to 100 nA particle current). The entire vacuum system is operated by oil-free turbomolecular pumps and dry roughing pumps to minimize hydrocarbons in the residual gas. We used a beam current of about 500 pA or less, with a beam collimator size of 0.5 mm, resulting in a beam spot of about 2.5 mm diameter on the sample. The pressure in the chamber was 10^{-9} Pa.

Hydrogen is detected by a nuclear reaction with the ^{15}N ion beam, resulting in an alpha particle and a gamma ray of 4.4 MeV, which is then detected. The reaction cross section has an energetically narrow resonance (at the ion beam energy of 6.4 MeV) and the detected hydrogen comes from a narrow layer within the material. Depth profiles can be obtained by increasing the beam energy above the resonance energy. Here, the ion beam loses energy by passing through the sample before the resonance energy is reached (Landford, 1992). Depth resolution of a few nanometers is achieved near the surface, and continuously decreases with depth to ~70 nm at 2 µm depth. Additional uncertainty arises if the sample surface is not perfectly flat. The method yields the absolute hydrogen concentration relative to other atoms. The composition of the target material, obtained from other methods, is used as input parameter in the SRIM software (Ziegler, 2004) in order to accurately compute the corresponding stopping power. This latter value allows to convert the incoming energy value into a depth information and the gamma ray translates into

H content (a more detailed description of the method can be found in Landford (1992)). Given that our studied materials are beam sensitive, we had to evaluate the damage rate under different conditions and to establish a method to correct for this effect. To that end, we measured two reference materials (serpentine and montmorillonite) and determine their beam damage rates; the results are presented in the appendix.

2.2.4. Focused ion beam (FIB)

To perform TEM and STXM analysis, it is required to have samples, which are transparent to electrons and X-rays. The focused ion beam technique allows preparing 100 nm thin sections (20 x 5 µm large) with preserved phase relationships. We used a single beam device (FEI FIB 200) operated at GFZ Potsdam. The FIB Ga ion milling was carried out at an ion beam voltage of 30 kV. Milling at low Ga-ion currents at the final stages minimizes common artifacts like local gallium implantation, mixing of components, creation of vacancies or interstitials, creation of amorphous layers, local compositional changes or redeposition of the sputtered material on the sample surface (Rubanov and Munroe, 2004; Obst et al., 2005; Langford, 2006; Drobne et al., 2007; Mayer et al., 2007). Thin sections were lifted out ex situ with a micromanipulator and transferred to a TEM grid.

2.2.5. Transmission electron microscopy (TEM)

Transmission electron microscopy and STXM spectroscopic observations is a powerful combination of techniques as the same FIB section can be used for both, and the deducted information spatially correlated (Bernard et al., 2010, 2012; Bourdelle et al., 2013; De Gregorio et al., 2013; Le Guillou et al., 2013, 2014). The TEM study was carried out at the University of Münster using a 200 kV Zeiss Libra®200FE with Köhler illumination, equipped with a Noran System Six EDS system and an in-column energy filter. Measurements were performed using STEM/EDS on the Libra by rastering over the regions of interest (<100 nm x 100 nm). Further high resolution and energy dispersive spectroscopy (EDS) investigations have been performed on a Jeol 3010 (300 kV acceleration voltage, LaB_6 electron source) equipped with an Oxford Isis EDX system. Quantification of the EDS data was conducted using the Cliff–Lorimer thin film approximation with experimentally determined k-factors for major elements (Mg, Fe and Si).

2.2.6. Scanning transmission X-ray microscopy (STXM)

Scanning Transmission X-ray Microscopy (STXM) is a transmission spectromicroscopy technique using a synchrotron radiation (Kilcoyne et al., 2003). It allows imaging at the 25-nm scale with speciation sensitivity and spectroscopic measurements - i.e. recording X-ray absorption near edge structure (XANES) spectra. For imaging, the X-ray beam is focused on the sample, and a 2-D image is collected by scanning the sample at fixed photon energy. The image contrast results from differential absorption of X-rays, which depends on the speciation of the

element of interest (iron valency at the Fe-$L_{2,3}$ edge). XANES spectra can be obtained by collecting stacks of images at increasing energy. The spectral resolution was 0.15 eV for the key energy ranges, i.e. between 705 and 712 eV and between 718 and 725 eV.

Measurements were done using the STXM located on beamline 10ID-1 at the Canadian Light Source (CLS, SM beamline - Kaznatcheev et al., 2007). Beamline 10ID-1 (CLS) uses soft X-rays (130-2500 eV) generated with an elliptically polarized undulator (EPU) inserted in the 2.9 GeV synchrotron storage ring (250-100 mA). The microscope chamber was evacuated to 13.3 Pa after sample insertion and back-filled with He. Dwell time was one millisecond per pixel. The absorption images of the stack were aligned using the automated image alignment routine of the aXis2000 software (ver2.1n - available on http://unicorn.mcmaster.ca/aXis2000.html) which was also used to extract XANES spectra from image stack measurements. Quantification of the $Fe^{3+}/\sum Fe$ ratio was performed using calibrations established on standards of known compositions (Bourdelle et al., 2013; Le Guillou et al., 2015).

3. Combining analyses: analytical sequence for characterization of multi-layers systems at the nanoscale

To obtain a complete characterization of the reacted solids, we developed a sequence of analysis to optimally combine SEM, FIB/TEM, RBS, NRA and STXM. Individually, each of these methods is well established in material sciences and geosciences. However, to the best of the authors's knowledge, they have never been combined in such an integrated manner. The novelty of our approach is to use the information brought by each individual technique to fully exploit the information obtained by the others and create an internal, iterative feedback. The analytical sequence is also designed to minimize sample damage. After the alteration reaction, the samples typically consist of a succession of distinct layers whose physical properties are needed to understand the alteration mechanisms. In the following, we present the characterization sequence using the example of the starting material prior to the alteration experiment (Table 1, Fig. 3, 4), i.e. the film deposited from a fayalite 50 olivine target:

1) Imaging the film surface by SEM provides the morphology of the film surface, and allows assessing the **fine scale structures** in weakly reacted samples, as well as the lateral heterogeneities. The starting material shows a planar surface at the sub-micrometer scale, free of defects and irregularities (see Fig. 4c in Dohmen et al., 2002).
2) Extracting thin foils using the FIB technique (Fig. 3a). This must be done before NRA to avoid irreversibly damage of the sample (see appendix).
3) Performing STXM analyses of the thin foils (30 nm pixel size). STXM allows quantitative mapping of the **iron redox state**. The starting thin film consists of a pure Fe^{2+} silicate (Fig. 3b). Knowledge of the $Fe^{3+}/\sum Fe$ ratio is required to **balance the stoichiometry** of the reacted silicates, which in turn is needed to interpret the RBS and NRA raw data. It also offers the possibility to investigate the ongoing oxidation reaction. Note that this

must be done before TEM, which potentially damages the sample by either amorphization or Fe reduction under vacuum.

4) Performing TEM analyses (nanometer resolution) to obtain several key information:
    a. **Layer thicknesses** (required for RBS and NRA treatment) and **textures.**
    b. **Layer composition and compositional zoning** using EDS mapping or energy filtered imaging. Most major elements can be measured with 2% precision, and oxygen can be estimated at 10-15 % precision (Le Guillou and Brearley, 2014)
    c. **Crystallography** (amorphous vs. crystalline, phase determination, etc…).
5) Performing RBS measurements to determine compositional depth profiles of major elements:
    a. The elementary analysis and the Fe^{3+}/Fe^{2+} ratio obtained by TEM and STXM provide a first estimation of the layer composition, which can be used as a initial input to fit the measured RBS spectra. The latter ultimately provides a laterally **averaged elementary composition** of each layer.
    b. Using the layer thickness obtained by TEM, the **density** of each layer can be deduced

At this stage (i.e., before NRA), the best fit obtained from the RBS spectra yields an extracted composition of $Fe^{2+}_{1.1}Mg_{0.9}SiO_4$ (Fig. 3c). The composition is homogeneous at depth. The film has a density of ~ 3.9 $g \cdot cm^{-3}$, which is the same as that of olivine of the same composition.

6) Performing NRA measurements (beam width: 1 mm; depth resolution: ~ 20-100 nm). The samples are large enough to analyze a region not previously damaged by the RBS beam. Several steps are needed to treat the NRA data:
    a. Establish the H loss behavior by performing several measurements at a given energy (~ depth) using the lowest beam current possible (~ 400 pA) and fit the H loss vs. deposited charge logarithmic function (see appendix). We performed this measurement at two different energies to account for the multi-layer nature of the reacted products. Correction for H loss can then be applied.
    b. Determine the stopping power of each layer using SRIM based on the element composition and density (obtained from TEM-RBS) in order to:
        i. Convert the nuclear reaction yield (gamma rays) into H content
        ii. Establish the energy-depth relationship to obtain a **depth-resolved H profile**.

For the present example of this starting material, no Hydrogen loss is observed with increasing charge, indicating that it is strongly bonded to the silicate structure, probably as hydroxyl groups. Using the composition deduced from RBS, we calculate a stopping power of 254 x 10^{-15} $eV \cdot at^{-1} \cdot cm^2$, which is used to convert the H yield into the observed H content and to establish the depth vs. energy calibration. Hydrogen is present at about 2 H_2O mol % and the concentration slightly decreases with depth (Fig. 3d). The presence of hydrogen is probably due to absorption (or reaction) of atmospheric water on unsaturated bonds leftover after condensation.

7) Re-processing the RBS fitting using the determined H concentration (and consequently adjusted stoichiometry) of each layer (step 5)
8) Refining the stopping power and depth calibration required for NRA analysis (step 6b) based on the adjusted RBS data. The final composition obtained for the starting material after the described iteration is $Fe^{2+}_{1.1}Mg_{0.9}SiO_{4.2}\ H_{0.4}$.
9) Calculating the **concentration of dissolved cations.** Knowing the composition, density and thickness of each layer, the final "bulk" solid composition can be determined. By comparison between the initial homogenous film composition and normalization to one element (e.g., Fe), the fluid elemental ratios (Si/Fe; Mg/Fe) can be deduced as well assuming a closed system and no precipitation of other phases within the Au cell.

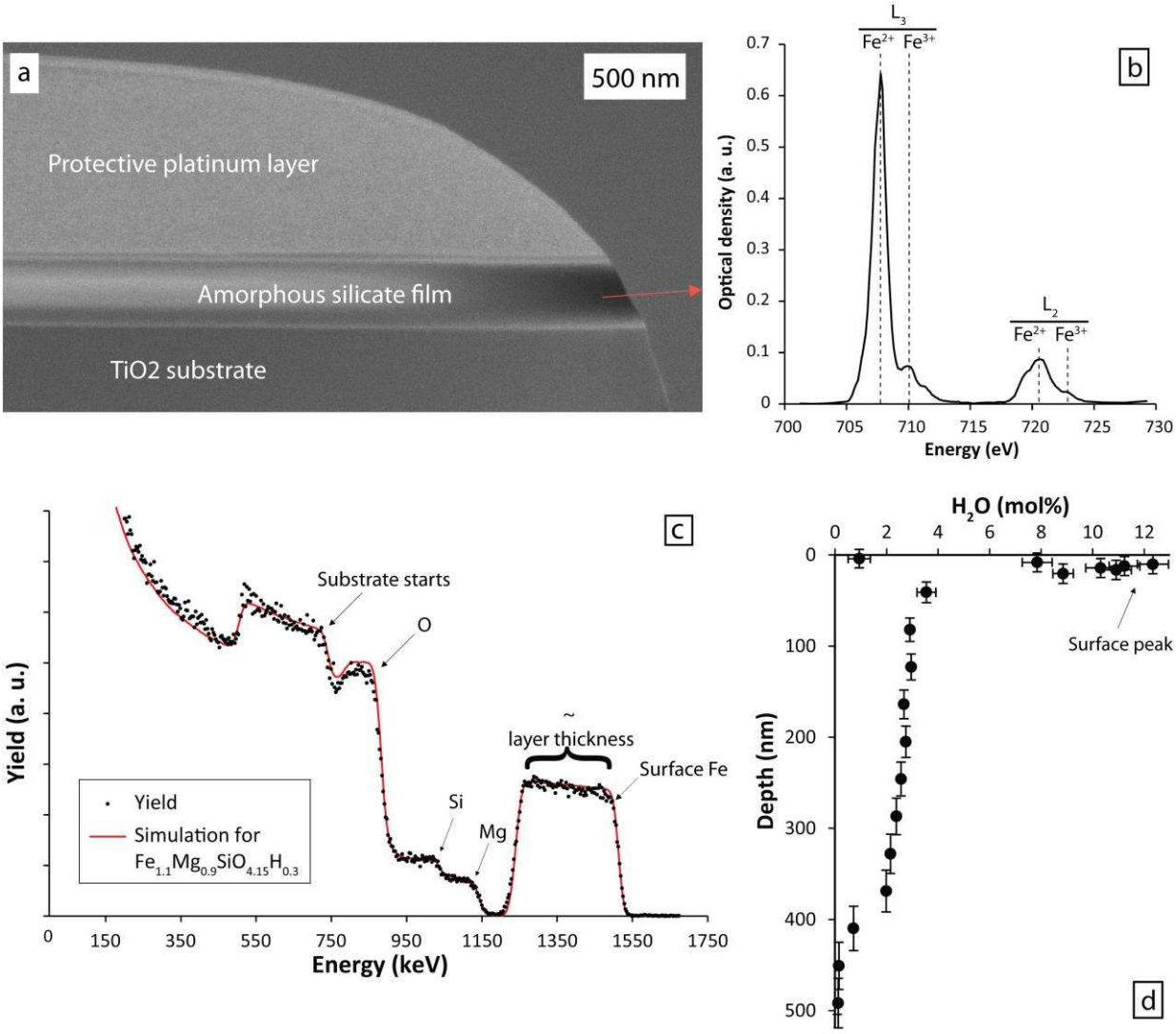

Fig. 3: a) SEM image of a FIB section cut from an amorphous silicate film right after deposition; b) XANES spectrum at the Fe-$L_{2,3}$ edge obtained by STXM on the same FIB section. The tiny absorption band centered around 710 eV is not due to the presence of Fe^{3+} in this case, but to electronic transitions related to phase specific coordination of Fe^{2+} (van Aken et al., 2002). Our

empirical calibration shows that the present spectrum is exactly the same as that of an olivine and corresponds to pure ferrous iron (Bourdelle et al., 2013; Le Guillou et al., 2015). The presence of a peak around 710 eV is also present in spectra of olivine standards and is not due to the presence of Fe^{3+}. In contrast, altered layers have significant Fe^{3+} peaks, as described below; c) RBS spectra (black points) and simulated spectrum (red) of a 400 nm thick layer of density 3.9 $g.cm^{-3}$ and composition $Fe_{1.1}Mg_{0.9}SiO_{4.15}H_{0.3}$; d) NRA hydrogen depth profile of the film, showing that hydrogen is present within the film (the actual value decreases from 2.7 to 2 H_2O mol%; errors bars are smaller than the dots for the in-depth analysis). We chose to present the data as H_2O content but we presently do not know the actual speciation of hydrogen in the starting material.

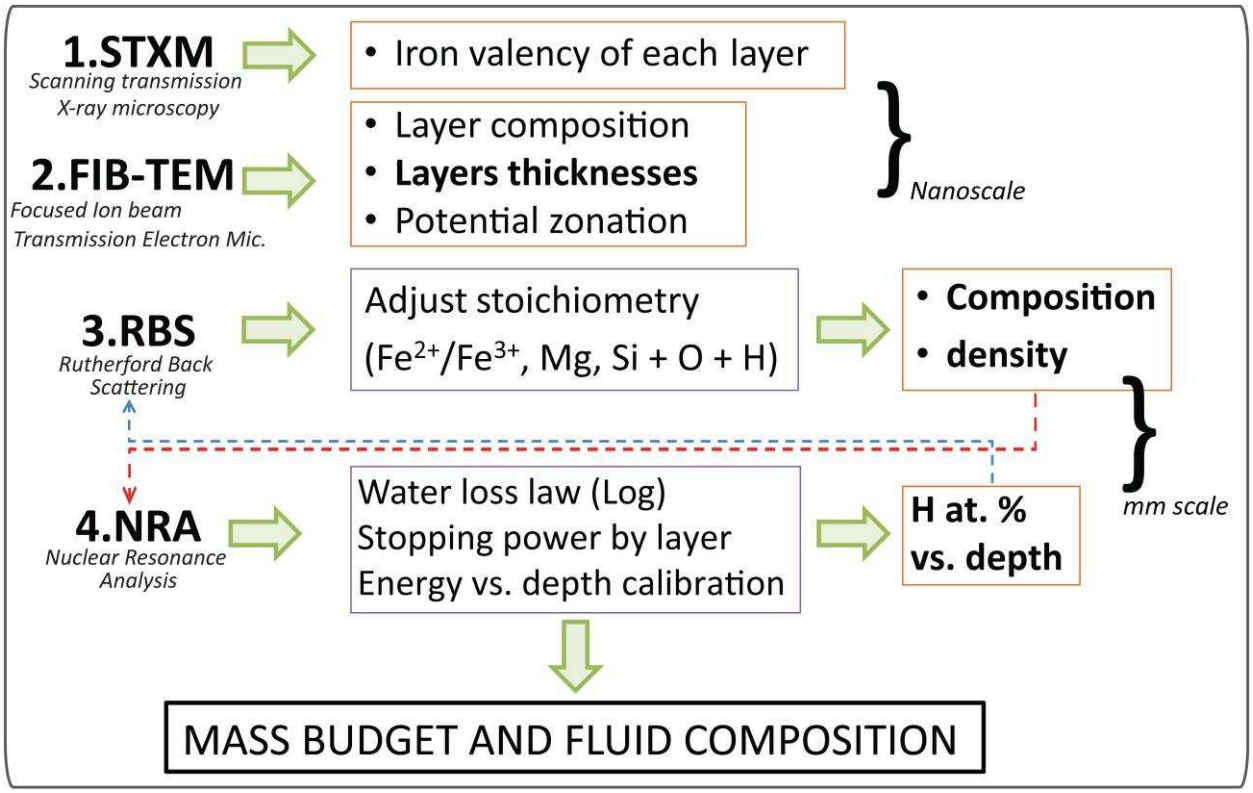

Fig. 4: Sequence of analytical methods used to characterize the reacted films, and physical/chemical parameters which can be deduced from each of them. Interpretations of the RBS and NRA data are inter-dependent of each other and require to be processed several times to obtain consistent results.

Samples	Temp. (°C)	Duration	Reacted thickness (nm)	Density ($g.cm^{-3}$) *(Fe-L/Mg-L)*	Mean Mg/Fe (at.)	H_2O (wt.%) *(Fe-L/Mg-L)*	Inner-layer composition	Outer-layer composition
Am-Fa55	n.a.	n.a.	n.a.	3.9	0.82	2	$Fe^{2+}_{1.1}Mg_{0.9}SiO_{4.2}H_{0.4}$	
Am-Fa55	90	2 weeks	680	3 / 1.7	0.5	5 / 9	$Fe^{2+}_{0.5}Fe^{3+}_{0.6}Mg_{0.25}SiO_{4.05}H_{0.8}$	$Fe^{2+}_{0.5}Fe^{3+}_{0.5}MgSiO_5H_{1.6}$
Am-Fa55	190	2 hours	370	2.7 / 1.7	0.22	13 / 18	$Fe^{2+}_{0.9}Fe^{3+}_{0.4}SiO_{5.3}H_{3.1}$	$Fe^{2+}_{0.35}Fe^{3+}_{0.25}Mg_{0.5}SiO_{4.75}H_{4.2}$
Cryst-Fa55	190	2 hours	50	n.a.	0.16	11.3	n.a.	n.a.

Table 1: Summary of the main parameters characterizing the starting material and the reacted products.

Estimation of the uncertainties for each analytical method depends on the individual samples and the number of layers formed. As observed by SEM, there are some lateral heterogeneities at the surface of the sample. This, in turn, implies that composition and thickness of the individual layers determined on micrometer sized FIB sections are not always in exact agreement with the RBS data, which yield a laterally averaged value at the millimeter scale. RBS and NRA have excellent depth resolution (~10 nm) near the surface of the films, but resolution continuously decreases with increasing depth, due to scattering effects (straggling). Ion implantation modelling indicates that the uncertainty in depth resolution increases up to ~ 70 nm at 2 µm depth. In addition, the surfaces of the samples have heterogeneous thicknesses because of the heterogeneous growth of secondary silicates, and therefore the RBS peaks are not as sharp as in an ideal case. As a result, the composition accuracy and the depth resolution are degraded. Since these data are used to determine the stopping power itself, which is required to obtain the H concentration depth profile from NRA, this uncertainty is propagated. Depending on the samples, these heterogeneities and related uncertainties are variable. However, combining all different techniques providing constraints on similar parameters and re-iterating using the internal feedback, ultimately leads to a consistent determination of the layers characteristics. Resulting uncertainties for the layer composition are estimated as follows: less than 3% on Fe and Fe^{2+}/Fe^{3+} ratio; less than 10% on Mg and Si; less than 15% for O and H; 20 nm precision on depth and layer thickness determination at the surface and 100 nm at greater depth; up to 30 % precision on the density determination for the very porous Mg-rich layers and down to 10% for the more compact, homogeneous layers.

4. Results: alteration of amorphous and crystalline thin film

4.1. Amorphous thin film alteration at 90 °C

After two weeks at 90 °C, the surface of the film is heterogeneously altered and SEM reveals morphologically different regions: i) flat regions, likely corresponding to less altered areas, ii) circular areas, covering most of the film, display nm-thick flakes which resemble phyllosilicates(Fig. 5a, b); iii) on top of the flakes, micrometer large patches are present. In depth,

the dark-field STEM image (Z number contrast) of the FIB section shows four different layers. They are all amorphous according to electron diffraction. Despite the fact that TEM can sometimes amorphize phyllosilicates, it occurs only after some exposition time if the beam is focused on a small region. In this case, diffraction was performed under low fluence rate and no crystalline phases were observed. The characteristic of the different layers formed are described below (Fig. 5c, d):

- The lower part consists of unreacted material,
- The inner layer, at the reaction front, shares a sharp boundary with the unreacted silicate, and consists of a 150 nm thick, hydrated and oxidized silicate. Its composition, close to that of serpentine, is $Fe^{2+}_{0.5}Fe^{3+}_{0.6}Mg_{0.25}SiO_{4.05}H_{0.8}$ and it has a density of ~ 3.5 $g.cm^{-3}$. The texture is homogeneous and compact, and no apparent porosity is visible,
- Above, a 200 nm thick layer with a roughly similar composition is found ($Fe^{2+}_{0.5}Fe^{3+}_{0.6}Mg_{0.3}SiO_{4.2}H_1$). It has, however, a slightly higher H content and also a lower density (~ 2.5 $g.cm^{-3}$).
- The outer layer consists of a Mg-rich silicate ($Fe^{2+}_{0.5}Fe^{3+}_{0.5}MgSiO_5H_{1.6}$), with a fibrous texture corresponding to the "flakes" observed by SEM. The thickness of this layer is variable. A mean value of 300 nm for a density of 1.8 fits well the RBS data.
- A 30 nm thick layer of averaged composition $Mg_{0.8}SiO_{4.4}H_{3.2}$ is required to fit the RBS data, but is not visible in the FIB section. It corresponds to the patches observed by SEM (Fig. 5 a, b). Its stoichiometry is close to that of saponite containing molecular water.

NRA suggests that the altered layers are all hydrated (8-13 mol% H_2O), with a decreasing water content with increasing depth. The STXM composite image obtained from the XANES spectra displays the iron valency in each layer (Fig. 5 e, f). The unreacted layer is 100% Fe^{2+}, the inner Fe-rich layer is the most oxidized one ($Fe^{3+}/\sum Fe = 54 \pm 3\%$) and the outer, lower density layer might be slightly less oxidized ($Fe^{3+}/\sum Fe = 50 \pm 3\%$).

The relative bulk composition of the altered film changes slightly compared to the starting material, with the addition of water (6 wt.%) and the loss of Mg, which have likely been dissolved in the fluid. We calculate an averaged Mg/Fe value for the altered solid of 0.5 taking into account the composition, thickness and density of each layer.

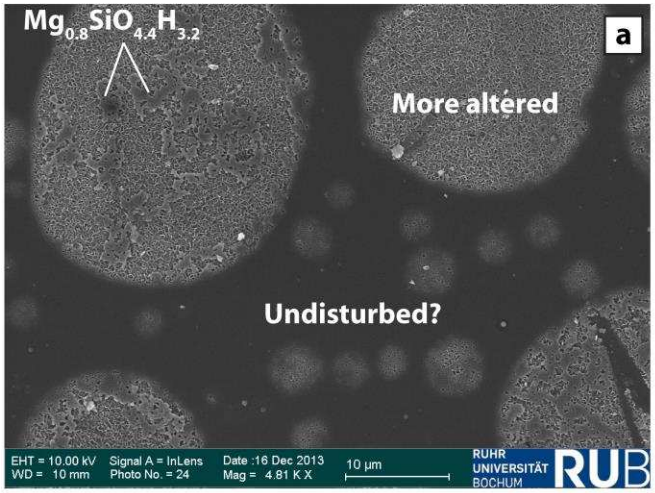
$Mg_{0.8}SiO_{4.4}H_{3.2}$
a
More altered
Undisturbed?
EHT = 10.00 kV
WD = 10 mm
Signal A = InLens
Photo No. = 24
Date :16 Dec 2013
Mag = 4.81 K X
10 µm
RUHR UNIVERSITÄT BOCHUM
RUB

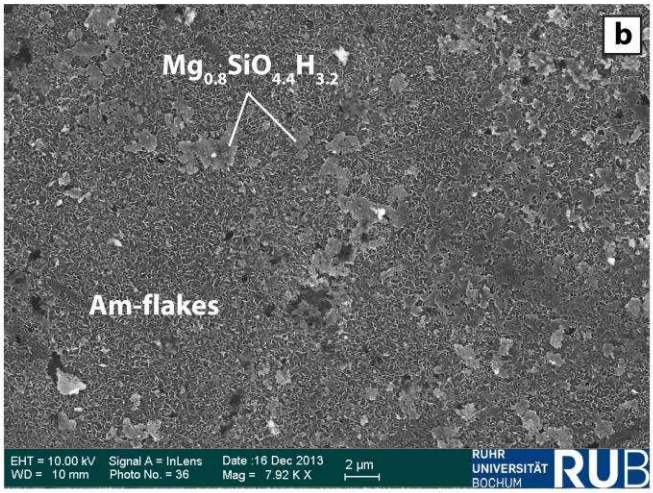
b
$Mg_{0.8}SiO_{4.4}H_{3.2}$
Am-flakes
EHT = 10.00 kV
WD = 10 mm
Signal A = InLens
Photo No. = 36
Date :16 Dec 2013
Mag = 7.92 K X
2 µm
RUHR UNIVERSITÄT BOCHUM
RUB

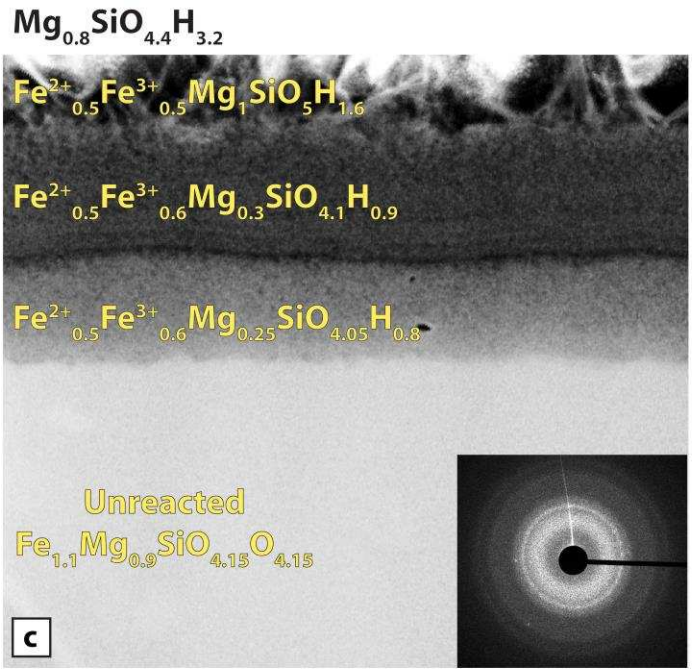
$Mg_{0.8}SiO_{4.4}H_{3.2}$
$Fe^{2+}_{0.5}Fe^{3+}_{0.5}Mg_1SiO_5H_{1.6}$
$Fe^{2+}_{0.5}Fe^{3+}_{0.6}Mg_{0.3}SiO_{4.1}H_{0.9}$
$Fe^{2+}_{0.5}Fe^{3+}_{0.6}Mg_{0.25}SiO_{4.05}H_{0.8}$
Unreacted
$Fe_{1.1}Mg_{0.9}SiO_{4.15}O_{4.15}$
c

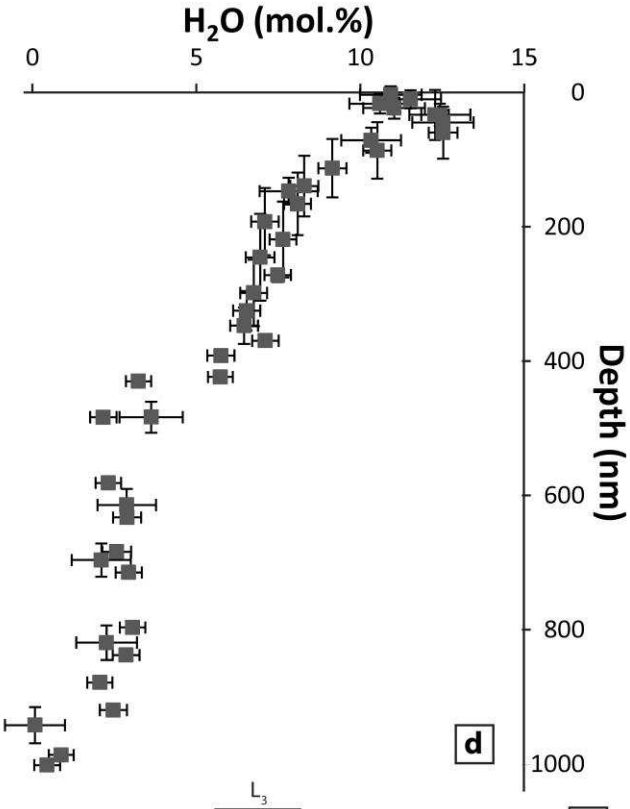
H_2O (mol.%)
0
5
10
15
0
200
400
600
800
1000
Depth (nm)
d

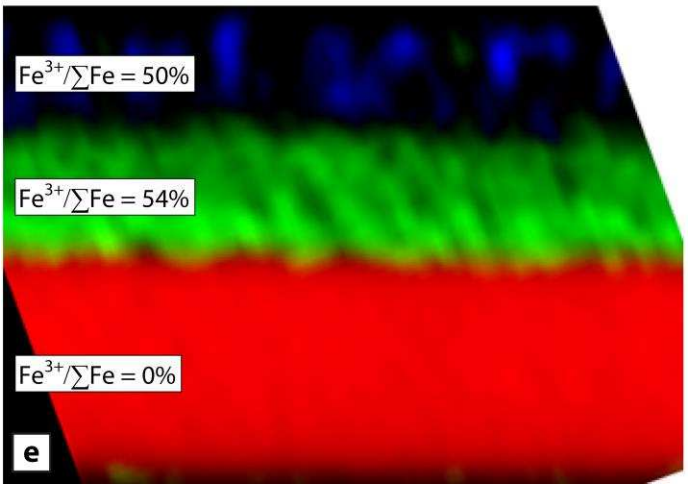
$Fe^{3+}/\sum Fe = 50\%$
$Fe^{3+}/\sum Fe = 54\%$
$Fe^{3+}/\sum Fe = 0\%$
e

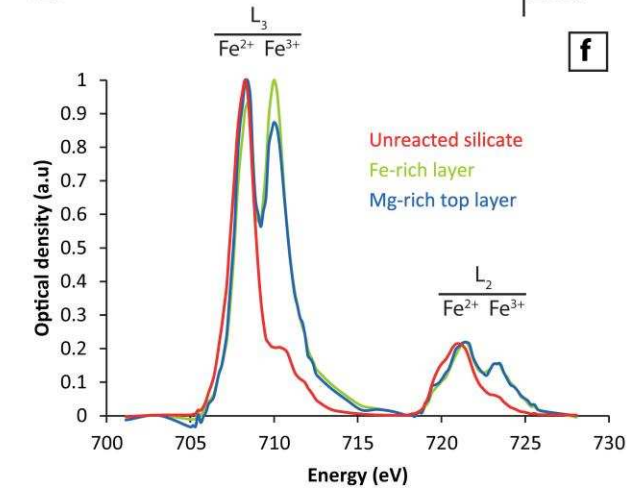
f
$\frac{L_3}{Fe^{2+}\ Fe^{3+}}$
$\frac{L_2}{Fe^{2+}\ Fe^{3+}}$
Unreacted silicate
Fe-rich layer
Mg-rich top layer
Optical density (a.u)
0
0.1
0.2
0.3
0.4
0.5
0.6
0.7
0.8
0.9
1
700
705
710
715
720
725
730
Energy (eV)

Fig. 5: a, b) SEM images of the surface of the film reacted two weeks at 90 °C. It is heterogeneous with regions showing less alteration, regions with 100 nm thick flakes and sometimes patches or pellicle of composition $Mg_{0.8}SiO_{4.4}H_{3.2}$; c) dark-Field STEM image of a FIB section extracted from an altered region. The Fe content and density decrease from the bottom (unreacted material) to the top. The scale is adjusted to that of the H_20 content depth profile; selected area electron diffraction of the Mg-rich layer, showing its amorphous nature; d) H_2O depth profile obtained by NRA showing the increasing hydration degree of the film from the bottom to the outer part; e) RGB map of the same FIB section obtained by STXM and corresponding to the spectra presented in f), normalized XANES spectra of the ferrous unreacted starting material and the oxidized outer layers.

4.2. Comparing amorphous and crystalline silicate reactivity at 190 °C

Olivine serpentinization has been studied at temperature above 200 °C (Martin and Fyfe, 1970; Wegner and Ernst, 1983; Marcaillou et al., 2011; Malvoisin et al., 2012a, b; Malvoisin and Brunet, 2014), but the behavior of amorphous silicate of similar composition remains mostly undescribed. With our experimental setup, we can directly compare the alteration behavior and their rates of crystalline and amorphous silicates with the same stoichiometry. To that end, we annealed an amorphous film in an atmosphere controlled furnace at 900 °C to form a polycrystalline aggregate. We then altered this film as well as an amorphous one, at 190 °C for 2 hours, in initially deionized water which was initially set to pH ~ 9 (Table 1).

Major differences are observed (Figs. 6, 7). SEM imaging shows that different micrometer sized regions of the crystalline film have a different alteration texture, with heterogeneous dissolution features (Fig. 6b). In contrast, the amorphous film has a homogeneous surface at the micrometer scale with typical roughness of 100 nm (Fig. 6d,e,f). The crystallized film is almost not altered (reacted thickness < 50 nm), whereas about 400 nm of the amorphous film are transformed – but the products have different densities, and reacted mass are not directly comparable (Fig. 7). The resulting alteration texture of the different starting materials is also different. The surface of the crystalline film shows a thin layer (50 nm) of amorphous hydrated silicon oxide. The latter is intermixed with an amorphous material with a cation ratio similar to saponite (Fig. 8). In contrast, the amorphous film has been transformed into two distinct amorphous and hydrated layers. The outer layer shows some porosity and has a fibrous texture. It can be subdivided into two regions. The top region consists of a pure Mg-rich silicate ($Mg_{0.8}SiO_{4.9}H_{4.2}$), which evolves towards a more iron-rich composition ($Fe^{2+}_{0.3}Fe^{3+}_{0.3}Mg_{0.5}SiO_{4.7}H_{2.9}$). For this particular sample, we did not measure the Fe^{3+}/Fe^{2+} ratio, and the compositions are calculated assuming that each layer has roughly the same iron valency as observed in other samples altered at different temperatures or duration, e.g. around 50% for the Mg-rich layer and around 70% for the Fe-rich layer. The inner layer is texturally compact and

homogeneous. It consists of an Fe-rich silicate with a stoichiometry (including H content: ~ 15 mol% H_2O) close to that of serpentine ($Fe^{2+}_{0.4}Fe^{3+}_{0.9}SiO_{5.3}H_{3.1}$). The boundary between the different regions is sharp (< 20 nm). The outer Mg-layer contains additional water, indicating that molecular water is also present. The bulk composition of the reacted amorphous film, when both layers are averaged, is depleted in Mg relative to Fe, indicating that some Mg has been lost to the fluid (Mg/Fe decreased from from 0.86 to 0.22 after alteration).

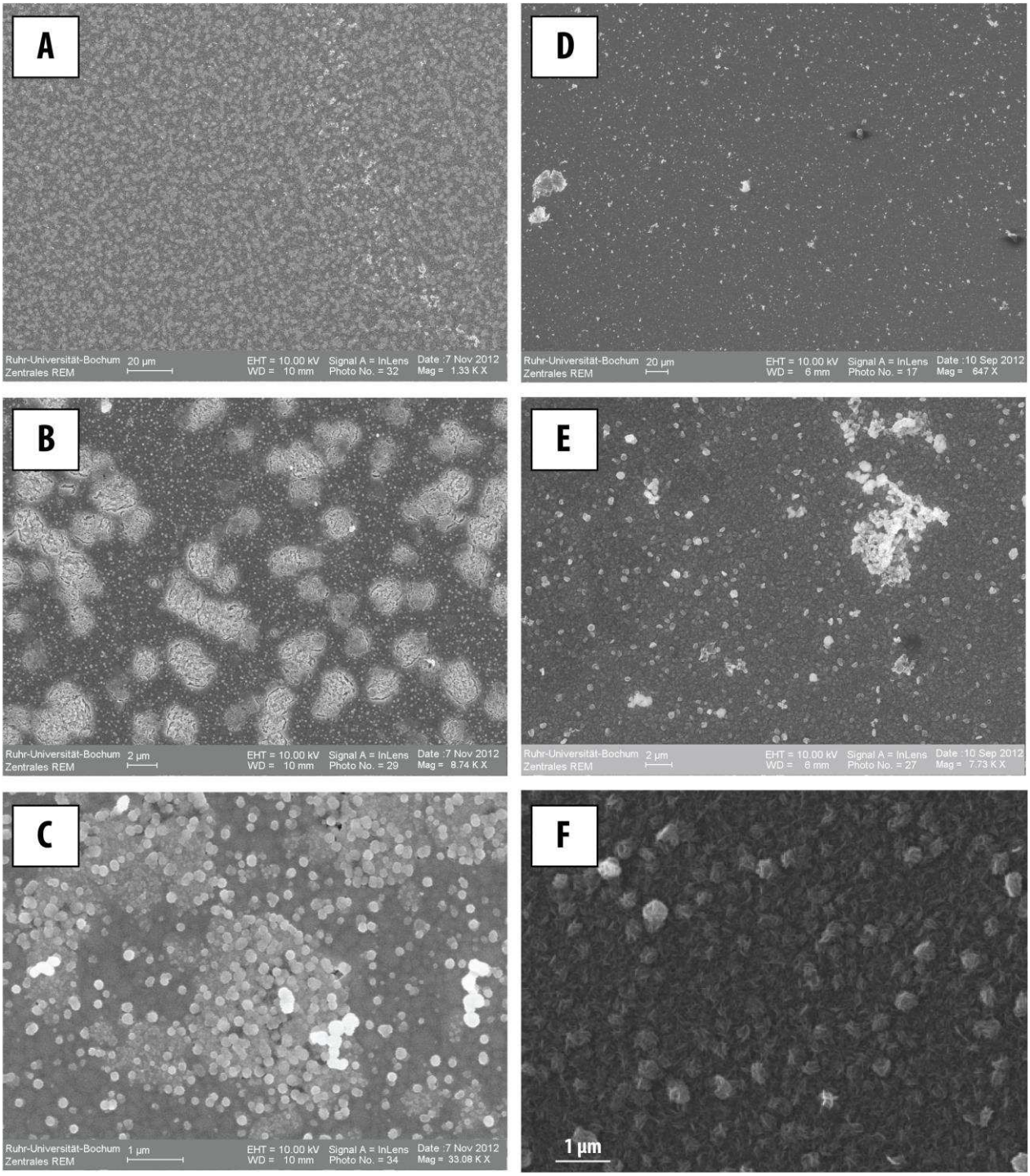

Fig. 6: SEM images of the crystalline film (a, b, c) and of the amorphous film (d, e, f), after reaction at 190 °C for 2 hours. The crystalline film shows heterogeneous alteration at the micrometer scale whereas the amorphous film reacts in a more homogeneous manner.

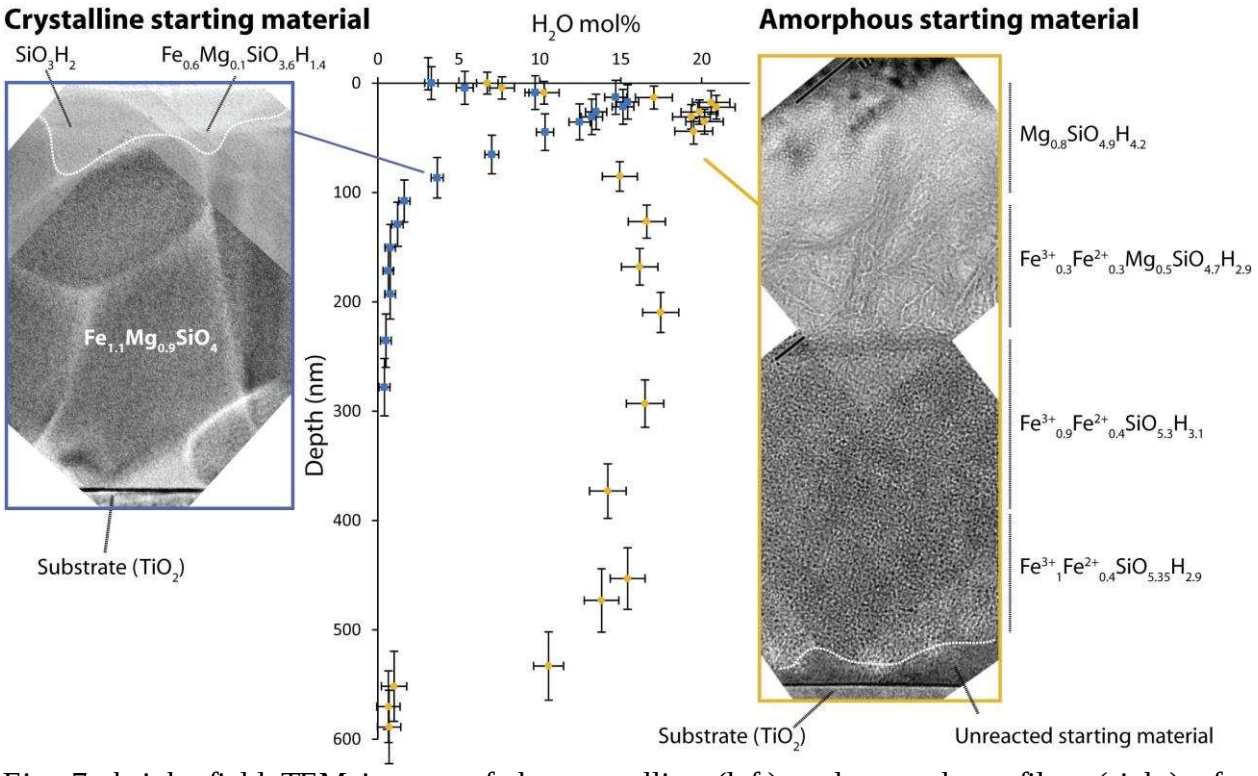

Fig. 7: bright field TEM images of the crystalline (left) and amorphous films (right) after reaction at 190 °C for 2 hours. The scale is given by the water content depth profile (central). The layers composition deduced from TEM, RBS and NRA show the chemical fractionation of the amorphous film. The thickness of the reacted hydrated material is much lower for the crystalline film than for the amorphous one. The altered amorphous film consists of two amorphous layers with different textures and compositions. A thin layer of the starting material can still be seen at the contact with the substrate.

5. Discussion: Alteration process in amorphous silicate of olivine composition

5.1. Reaction mechanisms of the amorphous condensate

The debate on the mechanisms of crystalline silicate dissolution has been mainly focused around two different scenarios (Berger et al., 1987; Hellmann et al., 2012; Daval et al., 2013; Ruiz-Agudo et al., 2014). One hypothesis is that the initial rate of the alteration is controlled by solid-state volume interdiffusion of protons and soluble cations, coupled with hydrolysis. This process has been called the "leached layer" mechanism and is associated with incongruent dissolution (Banfield et al., 1995; Crovisier et al., 2003; Gin et al., 2015). Alternatively, it was suggested that the overall rate is controlled by dissolution-precipitation at the interface between the primary material and, initially, the fluid (O'Neil and Taylor, 1967; Hellmann et al., 2003; 2012). Early on, a thin layer of water would become saturated with respect to secondary phases

(possibly metastable) whereas the "bulk" fluid remains undersaturated, due to slow transport of cations in the fluid phase. This phenomena would prevent homogenization of the fluid at the bulk scale, and thus induce a local oversaturation and nucleation of secondary phases (Ruiz-Agudo et. al, 2014 and reference therein). In this case, congruent dissolution is assumed. Precipitation would maintain the concentration of dissolved species at the interface between the primary and the secondary phase at a level that is sufficiently low to allow further dissolution, and this front would consequently migrate inward the starting material. In some cases, an amorphous Si-rich phase forms at the interface with the fluid, and thus, the solubility product and general properties of this amorphous layer also controls the overall dissolution rate (Daval et al., 2009, 2013). This mechanism has been called "interface-coupled dissolution-precipitation" (O'Neil and Taylor, 1967; Hellmann et al., 2003; 2012, 2015; Putnis et al., 2009; Ruiz-Agudo et. al, 2014).

Mechanisms of glass alteration have also been studied (Berger et al., 1987; Techer et al., 2001; Crovisier et al., 2003; Frugier et al., 2008; Valle et al., 2010; Parruzot et al., 2015). Our condensed amorphous silicate behave in many ways in a similar manner as borosilicates glasses (used for nuclear waste confinement) or as basaltic glass. In the latter cases, an inner hydrated gel layer forms at the interface with the pristine material and is depleted in the most soluble elements, which was first interpreted as being due to diffusion controlled processes, similar to the leached layer model. However, Valle et al. (2010) noted that depending on the considered elements, diffusion profiles are not systematically observed and hence hydrolysis-condensation reactions as well as interface coupled dissolution-precipitation need to be invoked as well. However, as noted by Hellmann et al. (2004), analysis by large beam techniques (RBS, NRA, SIMS) have sometimes led to artificial "diffusion profiles" which were due to analytical artefacts, and TEM only (or atom probe, Hellmann et al., 2015) has the resolution to assess the existence – or the absence - of a diffusion profile, a key to decipher between the different alteration models. In addition, in (partially) closed systems, precipitation of phyllosilicates on top of this inner gel layer has also been documented and its role in the element transfer processes must be taken into account (Crovisier et al., 2003; Valle et al., 2010). Porosity has then become an important parameter to understand the reactive mass transfer of water and cations through the inner layer and the precipitated phases (Cailleteau et al., 2008; Valle et al., 2010; Hellmann et al., 2012; Gin et al., 2013a,b; Daval et al., 2013).

At 190 °C and 90 °C, our condensed amorphous films exhibit a globally similar behavior. Indeed, the nature of each layer (compact and amorphous Fe-rich; fibrous and amorphous Mg-rich and thin Mg-Si rich crust) and the sharp boundaries between them indicate that the operating mechanisms does not change significantly within this temperature range. However, reaction rates are substantially different and the observed compositions of the resulting layers also vary with temperature (table 1; Fig. 8). A very unique feature compared to glass alteration studies is the presence of a sequence of four layers with different composition and oxidation state of Fe. At the reaction front, a Fe-rich amorphous, oxidized and hydrated layer forms. Its Mg/Fe ratio decreases with temperature (and/or possibly run duration), from initially 0.82 to 0.5 (90 °C, 2 weeks) and

0.22 (190 °C, 2 hours). It tends towards Fe-serpentine end-member. An outer Mg-rich layer develops at the surface with a texture resembling phyllosilicate flakes (Fig. 5, 6 and 7). At 190 °C, we observe a 80 nm thick Mg-Si-OH crust of saponite composition, an intermediate fibrous Mg-rich layer of intermediate stoichiometry and a front Fe-rich layer of serpentine stoichiometry. At 90 °C, the stoichiometry of both the Mg-rich and the Fe-rich layer is close to that of serpentine. Only the upper 30 nm thin layer is a pure Mg phase with a stoichiometry of saponite. However, in contrast to the 190 °C experiment, the H content is lower than in theoretical serpentine, showing that the transformation remains partial. The iron valency ($Fe^{3+}/\sum Fe$ ~55% at 90 °C, 2 weeks), determined in this kind of materials for the first time, indicates that the hydrolysis reaction is coupled to the oxidation of ferrous iron into ferric iron. Formation of the inner Fe-layer involves oxidation of ferrous iron to ferric iron following reaction such as Fe-silicate + water → $[Fe^{2+}/Fe^{3+}]$-phyllosilicate + magnetite + H_2. Magnetite does not always form, depending on the conditions, and if we establish the global equation of the reaction as well as the $Fe^{3+}/\sum Fe$ ratio of each layer, we can quantify the amount of H_2 produced during alteration and determine the related partitioning of Fe^{3+} between magnetite and phyllosilicates. At this scale, only STXM allows to quantify the Fe^{3+} content of each individual layer (Bourdelle et al., 2013; Le Guillou et al., 2015). Obtaining these information is crucial to understand the processes of oceanic floor serpentinization and hydrogen generation capabilities (Evans, 2008; Klein et al. 2009; Marcaillou et al., 2011; Malvoisin et al., 2012a, b) as well as for asteroids, for which H_2 asteroid degassing is involved (Alexander et al., 2010; Le Guillou et al., 2015).

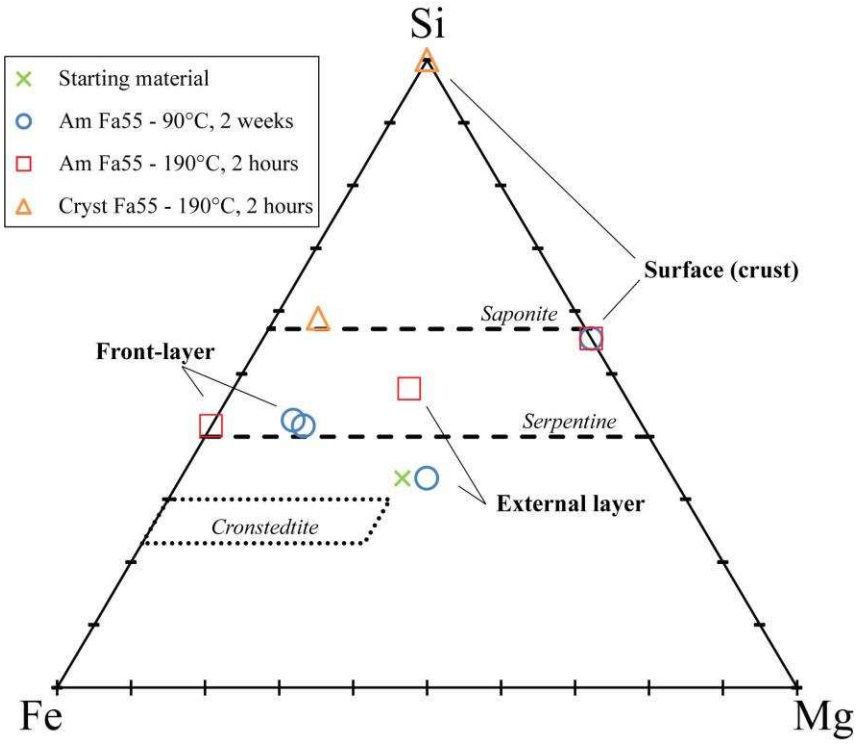

Fig. 8: Fe-Mg-Si ternary diagram (at.%) showing the composition of the layers at different temperature and comparing their stoichiometry to serpentine, saponite and cronstedtite. The fibrous outer layers are usually more Mg and Si rich, whereas the inner layers at the contact with the pristine material are Fe-rich and contain a little less Si.

Combining the various analyses, we can determine the composition, density and volume fraction of each layer and therefore estimate the average composition of the altered solid fraction. Ratios are normalized to iron which is theoretically the less soluble element under these conditions, in particular as it is mainly present at ferric iron. At 90 °C, the Mg/Fe ratio of the altered solid has dropped to 0.5 compared to 0.82 initially (table 1). The Si/Fe, on the other hand remains constant within uncertainties. At 190 °C, the Mg/Fe has dropped to 0.2 and the Si/Fe also remains constant. In both cases, Mg seems to be much more soluble than Si and Fe. Thermodynamic calculations performed at $T \leq 200$ °C on harzburgite and dunite compositions at various water:rock ratios suggest that Mg is generally more soluble than Si and Fe (McCollom and Bach, 2009; Klein et al., 2009). The Mg depletion of the solid can therefore be explained by preferential dissolution at equilibrium.

Another important observation is that the Mg-rich outer layer is always amorphous (Fig. 6c). Valle et al., (2010), and Rajmohan et al., (2010) also observed the presence of flakes but had considered them crystalline based on their morphology. Our results emphasize that diffraction is mandatory to confirm the crystallinity of such phases. From a mechanistic point of view, it also implies that precipitation occurs without nucleation of crystalline phases. This material may be similar to the proto-serpentine described in direct precipitation experiments at 90 °C (Lafay et al., 2013). Further transformation of the silicate will have to occur at higher temperature or longer reaction duration to obtain crystalline phases. Similar behaviors are observed with carbonates, for which a hydrated amorphous phase is now recognized as the initial structure formed before crystallite nucleation (Politi et al., 2004). Solubility, porosity and dissolution rate of this amorphous Mg-silicate will be affected by its transient nature. Those physical parameters must therefore be carefully considered when modeling the overall reactivity.

In our experiments, the reaction interface between the prisitine silicate and the inner layer are sharp, and no diffusion profiles were observed. If present, they would have to be shorter than our analytical resolution which is a few nanometers for TEM-EDS on a FIB section, and tens of nanometers for the NRA hydrogen profiles. Hellmann et al. (2012) modeled hydrogen solid-state diffusion at 90 °C within amorphous Si-gel layers and suggested that it is too slow to be the rate controlling mechanism. In our case overall transformation rate of the film is likely controlled by interface coupled dissolution-precipitation at the interface between the pristine silicate and the Fe-rich gel (Hellmann et al., 2012; Ruiz-Agudo et al., 2014; Geisler et al., 2015), or by H_2O transport through the gel and the Mg-rich phase. In either case, magnesium, which is more soluble than other elements, is transported from the pristine silicate to the outer Mg-layer. Diffusion in a fluid, present in a speculative nanoporosity (not yet observed) have been invoked

as transport mechanism (Berger et al., 1987; Hellmann et al., 2012). TEM do not reveal any porosity in our samples, which implies that it must be much smaller than the thickness of the FIB section (100 nm). A density of 2.5 to 3 $g.cm^{-3}$ is found for the gel layer of the 90 °C experiment. This is roughly similar to the density of serpentine of equivalent composition and it indicates that the porosity cannot be of significant importance for this case. To summarize, we can distinguish two propagation fronts: i) water penetration coupled with Mg-loss and oxidation of iron, at the expense of the pristine film, and ii) growth, probably by precipitation from the fluid, of the amorphous Mg-rich phyllosilicates. This mechanism involves the transport of magnesium, from the amorphous silicate through the Fe-rich gel. To thoroughly identify the mechanisms and their rates, a detailed study encompassing temperature effects, time series and kinetic modeling will be presented in a future paper.

5.2 Comparing reaction rates of amorphous silicate to crystalline olivine and silicate glasses alteration

To the best of our knowledge, the lowest temperature at which olivine serpentinization experiments have been performed is 200 °C. The main reason for that is that the reaction rate is too slow at lower temperatures to produce observable results within laboratory timescales, when using bulk analytical techniques (Seyfried et al., 2007; Malvoisin et al., 2012b). Some experiments using dissolved elements as starting materials can lead to the formation of serpentine (Lafay et al., 2013) at lower temperatures, but they cannot, however, be used for the purpose of kinetics studies since they do not involve the replacement of a solid as starting material. However, there is clearly a need to experimentally determine rates below 200 °C, because alteration can occur at much lower temperatures in some oceanic hydrothermal fields. In chondrites, alteration temperatures are even below 100 °C. Our setup allows determining the very early stages of the reacted material formed from a polycrystalline film (fayalite 55 composition) at 190 °C. Within two hours, a 50 nm layer has been formed, as a result of a dissolution-precipitation process leading to an amorphous, hydrated Fe-Mg-Si-O-H bearing layer. Given the very short run duration of only 2 hours, we anticipate this result of the first experiment as very promising. In the future, longer experiments at lower temperatures will allow us to investigate the rates of crystalline olivine alteration which could then be applied to low temperature natural systems.

Our approach allows to study the role of the degree of crystallinity by comparing the reaction rates of two materials of similar composition and density. The integrated front propagation rate, deduced from the two hours experiment (the instantaneous rate changes with time) is an order of magnitude faster for the amorphous silicate than the crystalline one (25 nm/hour compared to 200 nm/hour). Several possibilities could account for this higher rate: i) the presence of a few at.% of hydrogen in the initial amorphous silicate, ii) its metastable nature which implies a higher free energy of formation, which in turn could lead to a higher hydrolysis

rate, or (iii) additional reaction pathways due to a different initial polymerization degree. For instance. Daval et al. (2013) demonstrated that the dissolution rate of diopside depends on the crystallographic planes. They tentatively interpreted this as the consequence of different local atom densities and coordination, a parameter related to the local polymerization degree of silicon.

Our experiments using amorphous silicates of olivine composition can also be compared to previous ones involving glasses (at 90 °C), in order to investigate the role of the composition and that of the synthesis method (condensation vs. quenching). However, several important differences between the experimental setups influence the reaction rates and prevent an accurate comparison. First of all, rates of alteration vary with time, as the reaction progresses. In general, the initial rates are much faster because the process is controlled by dissolution only, before the fluid becomes saturated (at least locally) and gel layers start to form (Frugier et al., 2008; Valle et al., 2010). At some later point in time, i.e., as the gel layer becomes less porous and the fluid is saturated, long term rates that are orders of magnitude smaller are found. Most experiments on glass alteration have been performed in an open system to simulate geological conditions. Therefore, the fluid composition is not only controlled by the reaction progress but also by the fluid renewal rate. Secondly, different precursor materials involve different surface to volume ratios and without a complete chemical modelling, which is beyond the scope of the present work, it makes the direct comparisons rather difficult. Lastly, most studies used the fluid concentration as a proxy of the extent of alteration to constrain an equivalent dissolution rate, whereas in our case, it is the thickness and composition of the reacted solid, which is investigated. With those limitations in mind, we can tentatively compare our results with the work of Valle et al. (2010) performed on borosilicate glasses at 90 °C, 2 weeks. Under the same conditions, 400 nm of our amorphous film are altered (Fe-gel + Mg-rich flakes). Overall, the integrated reaction rate after two weeks is comparable (but slightly higher), e.g. about 600 nm of altered materials are present. This second order difference could be due to the fact that in their experiment the fluid is continuously renewed, which maintains a higher chemical gradient and enhances dissolution rates. Textural and compositional differences are also observed. Due to the difference in the initial composition of the glass, elements behave in a different manner. For instance, they find a Fe-enriched phyllosilicate layer and a Fe-depleted gel whereas in our case, the opposite is observed. A better comparison of the respective reaction rate would require more experiments and a thorough, parameter by parameter investigation, which is beyond the scope of this study. The main point here is that similar first order rates are observed for quenched glasses and condensed amorphous material.

6. Implications

6.1 Experimental and analytical advantages of our method

The purpose of this work is to illustrate the advantages of a new experimental setup and analytical approach, as well as their complementarity with existing methods, for the study of

alteration reactions at low temperatures. It has always been difficult to obtain a complete picture of the textural and chemical evolution of the solids during alteration, although this knowledge is crucial to characterize the mechanisms and kinetic laws. Studies on glasses for nuclear waste confinement have principally focused on the fluid composition to discuss the evolution of the solid phases (Crovisier et al., 2003; Frugier et al., 2008, 2009). However, in this study we show that altered solid may consist of several layers with evolving composition, H content and density and characterizing this multi-layer system cannot be done from the fluid analysis alone. Taking advantage of the well-defined planar geometry of the deposited thin film and the combined analytical techniques, we can determine most characteristics of the altered solid phase: the propagation rate of the reaction fronts, the layer thickness, composition and texture, the nature of the interface between the layers, the chemical zoning, the iron redox state in each different layer, the water content, the porosity and the density. By mass balance, the composition of the fluid can also be estimated. Altogether, the full description of the characteristics of the material allows mechanisms, such as chemical reaction rate (hydrolysis or oxidation for instance), evolution of the porosity and element transports by diffusion or advection to be investigated. In particular, because of the importance of the gel layer in transport processes, determining its hydration degree is crucial. Thanks to the initially defect-free film and of the planar geometry, the surface to volume ratio is easily constrained. The reaction front between the pristine material and the Fe-rich gel layer is always flat and sharp, and the specific reaction rate can therefore be directly investigated. This is more difficult with other setups using powders as starting materials. Indeed, as the reaction progresses, grains become smaller, and cracks can develop along grain boundaries, continuously modifying the S/V ratio.

Serpentinization experiments involving the replacement of olivine are usually performed at temperatures above 250 °C, in order to reach sufficient reaction advancement to be able to characterize the products. However, in natural environments, alteration often occurs at lower temperature (in some oceanic hydrothermal fields for instance, but also in asteroids; Klein et al., 2009; Brearley, 2006), and since the mechanisms may differ, it is required to determine their specific kinetic laws. Our protocol allows investigating alteration at very low temperature, i.e. very low reaction rates, for which only nanometer-sized regions react.

Finally, the versatility of the PLD method allows synthesizing amorphous material of various compositions (and crystallinity), which is not always possible to do by quenching, especially with iron rich melts. Films can also be doped with trace elements of various solubility or compatibility for instance, which can be useful to investigate specific alteration reactions. Combined with the integrated analytical approach, the method is broadly applicable for terrestrial and cosmochemical studies.

6.2 Application to serpentinization reactions in cosmochemistry

Amorphous silicates are ubiquitous in pristine chondrites (Brearley et al., 1993; Greshake et al., 1997; Abreu and Brearley, 2010; Hewins et al., 2013; Floss et al., 2014 ; Le Guillou and Brearley 2014; Le Guillou et al., 2014; Le Guillou et al., 2015). These silicates are among the oldest materials in the solar system and have been exposed to hydrothermal alteration at low temperatures in the asteroids from which the chondrites originate. However, understanding their origin and reactivity has so far remained difficult because of the lack of appropriate experimental data. The conditions during alteration of chondrites differ from classical terrestrial environments such as continental surfaces or metamorphic rocks. The precursor is initially amorphous and the reaction likely occurs in a closed system (Brearley, 2006), at low water to rock ratio. Using the pulsed laser deposition technique, we can synthesize the starting material likely present at the time of the accretion of the asteroids (Nuth et al., 2005), which was later altered to different degrees. Our experiments reproduce two important aspects of this material: i) an amorphous Fe-rich and hydrated phase similar to that found in CR chondrites (Le Guillou and Brearley, 2014; Le Guillou et al., 2014; Le Guillou et al., 2015) and ii) the dichotomy between fine-grained Mg-rich phyllosilicates and coarse-grained cronstedtite in CM chondrites, each having different $Fe^{3+}/\sum Fe$ ratio (Lauretta et al., 2001; Zega et al., 2003; Brearley et al., 2006).

At present, the temperature (0 to 150 °C) as well as the timescales (minutes to millions of years) of the hydrothermal events in carbonaceous chondrites (CR, CM, CI, CO) have remained very poorly constrained. These first results already show that alteration occurs fast, at 90 °C, with respect to asteroidal heating timescales (millions of years). We will now conduct experiments using this protocol, at temperature down to 50 °C and using various composition and alteration conditions, in order to help establishing the kinetic laws of these processes and the conditions of alteration of chondrites parent body.

9. Appendix: Assessing NRA beam damage using serpentine and montmorillonite standards

To evaluate the precision of the NRA measurements and investigate the effect of ^{15}N beam damage on the hydrogen content determination, we measured 2 standard materials: a serpentine (14 mol% H_2O; equivalent to 22 H at.%) and a montmorillonite (26 mol% H_2O before heating, equivalent to 33 at% H) obtained from the geology museum of the RUB. Serpentine contains only structurally bounded hydroxyl groups in a 1:1 structure whereas montmorillonite contains both molecular interlayer water and hydroxyl groups (2:1 structure). The samples were pressed in a gold foil and mounted in the analysis chamber. Serpentine was analyzed at 4 different beam currents (0.8 nA, 5 nA, 12 nA, 100 nA) and at a constant energy (around 7 MeV; resonance at ~ 200 nm below the surface). The beam charge for each data point was increased from 20 nC at 0.8 nA to 2.4 µC at 100 nA. The montmorillonite sample was first heated under

vacuum to 150°C to desorb some of the molecular water. It was then measured at increasing beam current (1 nA, 5 nA, 15 nA, 50 nA and 100 nA) with similar beam charges per data point and a constant energy (7 MeV).

It can be seen in Fig. 9 that hydrogen is progressively lost in both minerals as the total fluence (or accumulated charge) increases. Seven H at.% are lost in serpentine and 11 H at.% (on a total of 24 H at.% initially) in montmorillonite. The phyllosilicates are damaged by the beam and H is lost probably as H_2 or H_2O. The aim is to be able to correct for H loss as a function of the total accumulated charge (or total fluence) for measurements of real samples. In serpentine and montmorillonite, H loss is best fitted by a logarithmic function. In addition to the total fluence, beam current (fluence rate) also controls the H loss rate and different log functions can be determined at different beam currents, which implies that different H loss mechanisms are operating. At low current (< 12 nA), the damages are most likely dominated by elastic interactions alone between the beam and the samples, whereas local heating may contribute as well at higher current. For the range of beam current and total fluence used to measure our experimental samples (400 pA -1 nA; total fluence lower less than 3 µC), the same mechanism applies and it can be fitted by one given function. The first measurement (lowest total charge, minimum damage) provides the best estimation of the initial "real" value and therefore has a strong influence on the fitted H-loss function. To acquire this first data point, a good compromise has to be found between measuring for a short time to avoid damages and measuring long enough to have reasonable counting statistics. For experimental samples, this compromise was set to a charge of about 0.01 µC.

Correction for water loss is done as follows: i) fit of a log function through the H vs. charge evolution; ii) determination of the initial H content, taken as the value of the log function at a charge equal to a tenth of the minimum charge seen by the sample; iii) then the difference between the initial value and the value measured at a given charge (the H loss vs. charge) is obtained at all charge and another log function is obtained; iiii) this function is used to determine the real H value (corrected for H loss) at any charge. The result for serpentine (13 ±1 mol%) is in agreement with the theoretical value (14 mol%). For montmorillonite, the measured value is ~12.5 mol% which indicates that 50% of the initial water was lost during pre-heating.

The main conclusion is that it is possible to correct for H loss if the log function of a given layer is determined first. In the following, we always measure first the H loss behavior of the experimentally synthesized sample - at different depths (e.g. for different layers). The appropriate correction can then be applied to the H concentration as a function of depth and total charge.

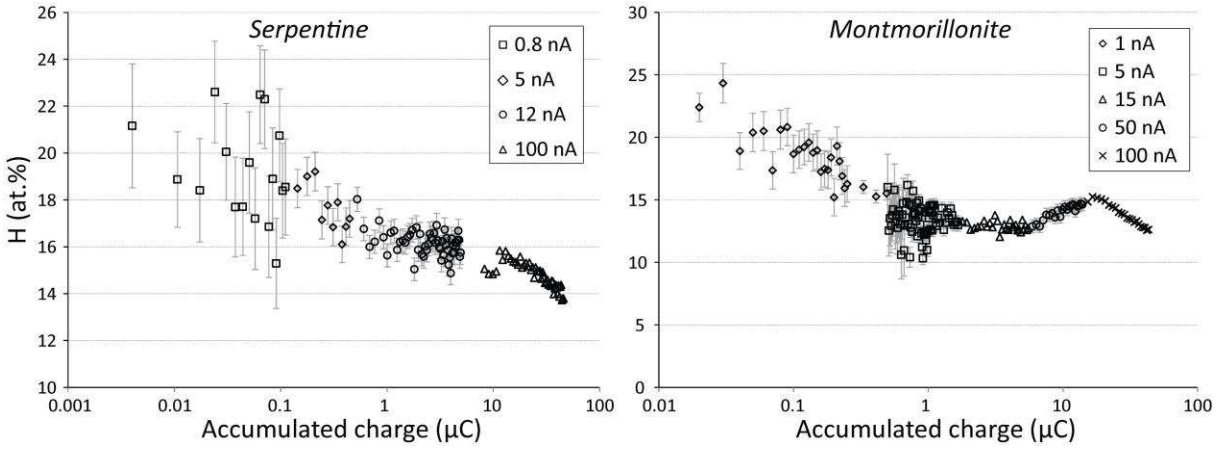

Fig. 9: Plot of the H content (at.%) vs. accumulated total particle charge (i.e the electrical beam charge normalized to the charge state of the ions) for both the serpentine (left) and the montmorillonite (right). At the lowest beam currents, the data form a straight line in a log scale. At higher beam current, there is a change in the mechanism controlling the H loss. Our experimental samples are always analyzed at current lower than 1 nA and the accumulated charge remains always below 3 µC.

7. Acknowledgments

Anja Schreiber (GeoForschung Zentrum, Potsdam, Germany) is warmly thanked for preparing the many FIB sections. Rolf Neuser is thanked for assistance with the SEM at the RUB. We would like to thank also the staff of the Tandem-Accelerator for support and help during the experiments. The SM beamline team at CLS (C. Karunakaran, J. Wang) is greatly acknowledged for the maintenance of the beamline. S.Bernard and J. Alleon from the french national museum of natural history are thanked for their help during STXM measurements. F. Bourdelle is also warmly acknowledged for developing the XANES calibration, which allowed quantification of the Fe^{3+} content. We also acknowledge the geology museum of the Ruhr University of Bochum for providing the serpentine and montmorillonite standards. The Deutsche Forschung Gemeinschaft (DFG) funded this work through the priority program "the first ten million years of the solar system" (SPP1385; grant # GU1298/1-1 to Corentin Le Guillou and Thomas Müller).

8. References

Abreu, N. M., Brearley, A. J., 2010. Early solar system processes recorded in the matrices of two highly pristine CR3 carbonaceous chondrites, MET 00426 and QUE 99177. Geochim. Cosmochim. Acta 74, 1146–1171.

Andreani, M., Muñoz, M., Marcaillou, C., Delacour A., 2013. μXANES study of iron redox state in serpentine during oceanic serpentinization. Lithos 178, 70–83.

Banfield, J.F., Ferruzzi, G.G., Casey, W.H., Westrich, H.R., 1995. HRTEM study comparing naturally and experimentally weathered pyroxenoids. Geochimica et Cosmochimica Acta 59, 19–31.

Benzerara, K., Menguy, N., Banerjee, N. R., Tyliszczak, T., Brown, G. E. Jr, Guyot, F., 2007. Alteration of submarine basaltic glass from the Ontong Java Plateau: A STXM and TEM study. Earth and Planetary Science Letters 260, 187–200.

Berger, G., Schott, J., & Loubet, M. (1987). Fundamental processes controlling the first stage of alteration of a basalt glass by seawater: an experimental study between 200 and 320 C. Earth and Planetary Science Letters, 84(4), 431-445.

Bernard, S., Benzerara, K., Beyssac, O., Brown, G. E. Jr., 2010. Multiscale characterization of pyritized plant tissues in blueschist facies metamorphic rocks. Geochim. Cosmochim. Acta 74, 5054–5068.

Bernard, S., Horsfield, B., Schulz, H-M., Wirth, R., Schreiber, A., Sherwood N., 2012. Geochemical evolution of organic-rich shales with increasing maturity: A STXM and TEM study of the Posidonia Shale (Lower Toarcian, northern Germany). Marine and Petroleum Geology 31(1), 70–89.

Bourdelle, F., Benzerara, K., Beyssac, O., Cosmidis, J., Neuville, D.R., Brown Jr., G.E., Paineau, E., 2013. Quantification of the ferric/ferrous iron ratio in silicates by scanning transmission X-ray microscopy at the Fe $L_{2,3}$ edges. Contrib Mineral Petrol 166, 423–434.

Bureau, H., Trocellier, P., Shaw, C., Khodja, H., Bolfan-Casanova, N., Demouchy, S., 2003. Determination of the concentration of water dissolved in glasses and minerals using nuclear microprobe. Nuclear Instruments and Methods in Physics Research B 210,449–454.

Brearley, A. J., 1993. Matrix and fine-grained rims in the unequilibrated CO3 chondrite, ALHA77307: Origins and evidence for diverse, primitive nebular dust components. Geochim. Cosmochim. Acta 57, 1521-1550.

Brearley, A. J. 2006. The action of water. In Meteorites and the Early Solar System II (eds. D. S. Lauretta and H. Y. McSween). University of Arizona Press, Tucson, pp. 587 – 624.

Cailleteau, C., Angeli, F., Devreux, F., Gin, S., Jestin, J., Jollivet, P., & Spalla, O. (2008). Insight into silicate-glass corrosion mechanisms. Nature materials, 7(12), 978-983.

Crovisier, J. L., Advocat, T., & Dussossoy, J. L., 2003. Nature and role of natural alteration gels formed on the surface of ancient volcanic glasses (natural analogs of waste containment glasses). Journal of Nuclear Materials 321(1), 91-109.

Daval, D., Martinez, I., Corvisier, J., Findling, N., Goffé, B., & Guyot, F., 2009. Carbonation of Ca-bearing silicates, the case of wollastonite: Experimental investigations and kinetic modeling. Chemical Geology 265(1), 63-78.

Daval, D., Hellmann, R., Saldi, G. D., Wirth, R., & Knauss, K. G., 2013. Linking nm-scale measurements of the anisotropy of silicate surface reactivity to macroscopic dissolution rate laws: new insights based on diopside. Geochimica et Cosmochimica Acta 107, 121-134.

Dohmen, R., Becker, H-W., Meißner, E., Etzel, T., Chakraborty S., 2002. Production of silicate thin films using pulsed laser deposition (PLD) and applications to studies in mineral kinetics. Eur. J. Mineral 14, 1155-1168.

Dohmen, L., Lenting, C., Fonseca, R. O., Nagel, T., Heuser, A., Geisler, T., and Denkler, R., 2013. Pattern Formation in Silicate Glass Corrosion Zones. International Journal of Applied Glass Science 4(4), 357-370.

Dorschner, J., & Henning, T., 1995. Dust metamorphosis in the galaxy. The Astronomy and Astrophysics Review, 6(4), 271-333.

Drobne, D., Milani, M., Leser, V., Tatti, F., 2007. Surface damage induced by FIB milling and imaging of biological samples is controllable. Microscopy Research and Technique 70(10), 895–903.

Evans, B. W., 2008. Control of the products of serpentinization by the $Fe^{2+}Mg_{-1}$ exchange potential of olivine and orthopyroxene. Journal of Petrology 49, 1873–1887.

Floss, C., Le Guillou, C., and Brearley, A., 2014. Coordinated NanoSIMS and FIB-TEM analyses of organic matter and associated matrix materials in CR3 chondrites. Geochim. Cosmochim. Acta, 139, 1-25.

Frugier, P., Gin, S., Minet, Y., Chave, T., Bonin, B., Godon, N., and Santarini, G., 2008. SON68 nuclear glass dissolution kinetics: Current state of knowledge and basis of the new GRAAL model. Journal of Nuclear Materials 380(1), 8-21.

Frugier, P., Chave, T., Gin, S., & Lartigue, J. E., 2009. Application of the GRAAL model to leaching experiments with SON68 nuclear glass in initially pure water. Journal of Nuclear Materials 392(3), 552-567.

Geisler, T., Nagel, T., Kilburn, M. R., Janssen, A., Icenhower, J. P., Fonseca, R. O., Grange, M., Nemchin, A. A., 2015. The mechanism of borosilicate glass corrosion revisited. Geochimica et Cosmochimica Acta, 158, 112-129.

Gin, S., Ryan, J. V., Schreiber, D. K., Neeway, J., & Cabié, M., 2013a. Contribution of atom-probe tomography to a better understanding of glass alteration mechanisms: Application to a nuclear glass specimen altered 25 years in a granitic environment. Chemical Geology 349, 99-109.

Gin, S., Frugier, P., Jollivet, P., Bruguier, F., and Curti, E., 2013b. New Insight into the Residual Rate of Borosilicate Glasses: Effect of S/V and Glass Composition. International Journal of Applied Glass Science 4(4), 371-382.

Gin, S., Jollivet, P., Fournier, M., Berthon, C., Wang, Z., Mitroshkov, A., Zhu,Z., Ryan, J. V.,, 2015. The fate of silicon during glass corrosion under alkaline conditions: a mechanistic and kinetic study with the international simple glass. Geochimica et Cosmochimica Acta 151, 68-85.

Godderis Y., Williams J. Z., Schott J., Pollard D. and Brantley S. L., 2010. Time evolution of the mineralogical composition of Mississippi Valley loess over the last 10 kyr: climate and geochemical modeling. Geochim. Cosmochim. Acta 74, 6357–6374.

Hellmann R., Penisson J.-M., Hervig R. L., Thomassin J.-H. and Abrioux M.-F., 2003. An EFTEM/HRTEM high-resolution study of the near surface of labradorite feldspar altered at acid pH: evidence for interfacial dissolution–reprecipitation. Phys. Chem. Miner. 30, 192–197.

Hellmannn, R., Penisson, J.-M., Hervig, R.L., Thomassin, J.-H., and Abrioux, M.F., 2004. Chemical alteration of feldspar: a comparative study using SIMS and HRTEM/EFTEM. In Water Rock Interaction (R.B. Wanty, R.R. Seal II, eds.), A.A. Balkema, Rotterdam, pp. 753-756.

Hellmann, R., Wirth, R., Daval, D., Barnes, J. P., Penisson, J. M., Tisserand, D., & Hervig, R. L., 2012. Unifying natural and laboratory chemical weathering with interfacial dissolution–

reprecipitation: a study based on the nanometer-scale chemistry of fluid–silicate interfaces. Chemical Geology 294, 203-216.

Hellmann, R., Cotte, S., Cadel, E., Malladi, S., Karlsson, L. S., Lozano-Perez, S. Cabié, M., Seyeux, A., 2015. Nanometre-scale evidence for interfacial dissolution–reprecipitation control of silicate glass corrosion. Nature materials 14, 307–311. doi:10.1038/nmat4172

Hewins, R. H., Zanda, B., Leroux, H., Barrat, J-A., Humayun, M., Göpel, C., Greenwood, R. C., Franchi, I. A., Pont, S., Lorand, J-P., Cournède, C., Gattacceca, J., Rochette, P., Kuga, M., Marrocchi, Y., Marty, B., 2013. The Paris meteorite, the least altered CM chondrite so far. Geochim. Cosmochim. Acta, doi:http://dx.doi.org/10.1016/j.gca.2013.09.014.

Hövelmann, J., Austrheim, H., Jamtveit, B., 2012. Microstructure and porosity evolution during experimental carbonation of a natural peridotite. Chemical Geology 334, 254-265.

Jones, C. L. and Brearley A. J., 2006. Experimental aqueous alteration of the Allende CV3 carbonaceous chondrite; Insights into asteroidal aqueous alteration. Geochimica et Cosmochimica Acta 70, 1040-1058.

Kaznatcheev, K. V., Karunakaran, C., Lanke, U. D., Urquhart, S. G., Obst, M., Hitchcock, A. P., 2007. Soft X-ray spectromicroscopy beamline at the CLS: commissioning results. Nuclear Instruments and Methods in Physics Research A 582, 96–99.

Kemper, F., Vriend, W. J., & Tielens, A. G. G. M., 2004. The absence of crystalline silicates in the diffuse interstellar medium. The Astrophysical Journal, 609(2), 826.

Kilcoyne, A. L. D., Tyliszczak, T., Steele, W. F., Fakra, S., Hitchcock, P., Franck, K., Anderson, E., Harteneck, B., Rightor, E. G., Mitchell, G. E., Hitchcock, A. P., Yang, L., Warwick, T., Ade, H., 2003. Interferometer-controlled scanning transmission X-ray microscopes at the Advanced Light Source. Journal of Synchrotron Radiation 10, 125–136.

Klein, F., Bach, W., Jöns, N., McCollom, T., Moskowitz, B., Berquo, T., 2009. Iron partitioning and hydrogen generation during serpentinization of abyssal peridotites from 15_N on the Mid-Atlantic Ridge. Geochim. Cosmochim. Acta 73, 6868–6893.

Knauss K. G., Johnson J. W., and Steefel C. I., 2005. Evaluation of the impact of CO2, co-contaminant gas, aqueous fluid and reservoir rock interactions on the geologic sequestration of CO2. Chem. Geol. 217, 339–350.

Kotai, E., 1994. Computational methods for analysis and simulation of RBS and ERDA spectra. Nucl. Instr. Meth. B 85, 588-596.

Lafay, R., Montes-Hernandez, G., Janots, E., Chiriac, R., Findling, N., Toche, F., 2013. Nucleation and Growth of Chrysotile Nanotubes in H2SiO3/MgCl2/NaOH Medium at 90 to 300 °C. Chem. Eur. J., 19, 5417 – 5424.

Landford, W. A., 1992. Analysis for hydrogen by nuclear reaction and energy recoil detection. Nuclear Instruments and Methods in Physics Research Section B: Beam Interactions with Materials and Atoms, 66(1), 65-82.

Lauretta D. S., Hua X., and Buseck P. R., 2000. Mineralogy of fine-grained rims in the ALH81002 CM chondrite. Geochim. Cosmochim. Acta, 64, 3263–3273.

Le Guillou, C., Bernard, S., Remusat, L., Leroux, H., Brearley, A.J., 2013. Amorphization and D/H fractionation of kerogens during experimental electron irradiation: comparison with chondritic organic matter. Icarus, 226, 101–110.

Le Guillou, C. and Brearley, A.J., 2014. Relationships between organics, water and early stages of aqueous alteration in the pristine CR3.0 chondrite MET00426. Geochim. Cosmochim. Acta, 131, 344-367, http://dx.doi.org/10.1016/j.gca.2013.10.024

Le Guillou, C., Bernard, S., Brearley, A.J., Remusat, L., 2014. Evolution of organic matter in Orgueil, Murchison and Renazzo during parent body aqueous alteration: in-situ investigations. Geochim. Cosmochim. Acta, 131, 368-392, doi: http://dx.doi.org/10.1016/j.gca.2013.11.020.

Le Guillou, C., Changela, H. G., & Brearley, A. J., 2015. Widespread oxidized and hydrated amorphous silicates in CR chondrites matrices: Implications for alteration conditions and H_2 degassing of asteroids. Earth and Planetary Science Letters, 420, 162-173.

Martin, B., Fyfe, W.S., 1970. Some experimental and theoretical observations on the kinetics of hydration reactions with particular reference to serpentinization. Chem. Geol. 6, 185–202.

Malvoisin, B., Carlut, J., Brunet, F., 2012a. Serpentinization of oceanic peridotites: 1. A high-sensitivity method to monitor magnetite production in hydrothermal experiments. Journal of geophysical research 117, doi:10.1029/2011JB008612.

Malvoisin, B., Brunet, F., Carlut, J., Rouméjon, S., Cannat, M., 2012b. Serpentinization of oceanic peridotites: 2. Kinetics and processes of San Carlos olivine hydrothermal alteration. Journal of geophysical research 117, doi : 10.1029/2011JB008842.

Malvoisin, B., and Brunet, F., 2014. Water diffusion-transport in a synthetic dunite: Consequences for oceanic peridotite serpentinization. Earth and Planetary Science Letters, 403, 263-272.

Marcaillou, C., Muñoz, M., Vidal, O., Parra, T., Harfouche, M., 2011. Mineralogical evidence for H2 degassing during serpentinization at 300 °C/300 bar. Earth and Planetary Science Letters 303, 281–290.

Mayer, J., Giannuzzi, L. A., Kamino, T., Michael, J., 2007. TEM sample preparation and FIB-induced damage. MRS Bulletin 32(5), 400–407.

McCollom, T. and Bach, W., 2009. Thermodynamics contraints on hydrogen generation during serpentinization of ultramafic rocks. Geochim. Cosmochim. Acta 73, 856–875.

Morlok, A. and Libourel, G., 2013. Aqueous alteration in CR chondrites: Meteorite parent body processes as analogue for long-term corrosion processes relevant for nuclear waste disposal. Geochim. Cosmochim. Acta 103, 76–103.

Mueller, T., Watson, E.B., Harrison, T.M., 2010. Applications of diffusion data to high-temperature earth systems, Reviews in Mineralogy and Geochemistry, 72, pp.997-1038. doi: 10.2138/rmg.2010.72.23

Nuth, III, J. A., Brearley, A. J., Scott, E.R.D., 2005. Microcrystals and Amorphous Material in Comets and Primitive Meteorites: Keys to Understanding Processes in the Early Solar System. Chondrites and the Protoplanetary Disk ASP Conference Series, Vol. 341, Eds. A. N. Krot, E. R. D., Scott, & B. Reipurth.

Obst, M., Gasser, P., Mavrocordatos, D., Dittrich, M., 2005. TEM-specimen preparation of cell/mineral interfaces by Focused Ion Beam milling. American Mineralogist 90(8-9), 1270–1277.

Ohnishi, I., & Tomeoka, K., 2007. Hydrothermal alteration experiments of enstatite: Implications for aqueous alteration of carbonaceous chondrites. Meteoritics & Planetary Science 42(1), 49-61.

O'Neil, J. R., & Taylor, H. P. (1967). The oxygen isotope and cation exchange chemistry of feldspars. American Mineralogist, 52, 1414-1437.

Parruzot, B., Jollivet, P., Rébiscoul, D., Gin, S., 2015. Long-term alteration of basaltic glass: Mechanisms and rates. Geochimica et Cosmochimica Acta 154, 28-48.

Pontoppidan, K.M., Brearley, A.J., 2010. Dust particle size evolution. In Protoplanetary Dust: Astrophysical and Cosmochemical Perspectives (Vol. 12). Apai, D., & Lauretta, D. S. (Eds.). Cambridge University Press, p191–229.

Putnis, A., 2009. Mineral Replacement Reactions. Reviews in Mineralogy & Geochemistry Vol. 70, pp. 87-124. doi: 10.2138/rmg.2009.70.3

Politi, Y., Arad, T., Klein, E., Weiner, S., and Addadi, L., 2004). Sea urchin spine calcite forms via a transient amorphous calcium carbonate phase. Science 306(5699), 1161-1164.

Rajmohan N., Frugier P., Gin S., 2010. Composition effects on synthetic glass alteration mechanisms: Part 1. Experiments. Chemical Geology 279, 106–119.

Rubanov, S., Munroe, P. R., 2004. FIB-induced damage in silicon. Journal of Microscopy 214(3), 213–221.

Rubin, A. E., Trigo-Rodriguez, J. M., Huber, H., Wasson, J. T., 2007. Progressive aqueous alteration of CM carbonaceous chondrites. Geochim. Cosmochim. Acta 71, 2361–2382.

Rudolph, W., Bauer, C., Brankoff, K., Grambole, D., Grötzschel, R., Heiser, C., & Herrmann, F., 1986. Plastic foils as primary hydrogen standards for nuclear reaction analysis. Nuclear Instruments and Methods in Physics Research Section B: Beam Interactions with Materials and Atoms, 15(1), 508-511.

Ruiz-Agudo, E., Putnis, C. V., & Putnis, A. (2014). Coupled dissolution and precipitation at mineral–fluid interfaces. Chemical Geology, 383, 132-146.

Schramm, B., Devey, C. W., Gillis, K. M., & Lackschewitz, K., 2005. Quantitative assessment of chemical and mineralogical changes due to progressive low-temperature alteration of East Pacific Rise basalts from 0 to 9 Ma. Chemical Geology 218(3), 281-313.

Seyfried, W. E. Jr., Foustoukos, D. I., Fu, Q., 2007. Redox evolution and mass transfer during serpentinization: An experimental and theoretical study at 200 °C, 500 bar with implications for

ultramafic-hosted hydrothermal systems at Mid-Ocean Ridges. Geochim. Cosmochim. Acta 71, 3872–3886.

Techer I., Advocat T., Lancelot J., Liotard J-M., 2001. Dissolution kinetics of basaltic glasses: control by solution chemistry and protective effect of the alteration film. Chemical Geology 176, 235–263.

Tomeoka, K., Buseck, P.R., 1988. Matrix mineralogy of the Orgueil CI carbonaceous chondrite. Geochim. Cosmochim. Acta 52, 1627–1640.

Traeger, F., Kauer, M., Wöll, C., Rogalla, D., Becker, H.-W, 2011. Analysis of surface, subsurface, and bulk hydrogen in ZnO using nuclear reaction analysis. Physical review B 84, 075462.

Valle, N., Verney-Carron, A., Sterpenich, J., Libourel, G., Deloule, E., & Jollivet, P., 2010. Elemental and isotopic ^{29}Si and ^{18}O) tracing of glass alteration mechanisms. Geochimica et Cosmochimica Acta 74(12), 3412-3431.

van Aken, P. A., Liebscher, B., 2002. Quantification of ferrous/ferric ratios in minerals: new evaluation schemes of Fe L2-3 electron energy-loss near edge spectra. Physics and Chemistry of Minerals 29, 188–200.

Watson, E. B., & Dohmen, R., 2010. Non-traditional and emerging methods for characterizing diffusion in minerals and mineral aggregates. Reviews in Mineralogy and Geochemistry 72(1), 61-105.

Wegner, W.W. and Ernst, W.G., 1983. Experimentally determined hydration and dehy-dration reaction rates in the system MgO–SiO_2–H_2O. Am. J. Sci. 283-A, 151–180.

Ziegler, J. F., 2004. SRIM-2003. Nuclear instruments and methods in physics research section B: Beam interactions with materials and atoms 219, 1027-1036.

Zega, T. J., Garvie, L. A. J., Buseck, P. R., 2003. Nanometer-scale measurements of iron oxidation states of cronstedtite from primitive meteorites. Am. Mineralog. 88, 1169–1172.

Zolensky, M. E., Bourcier, W. L., Gooding, J. L., 1989. Aqueous alteration on the hydrous asteroids: Results of EQ3/6 computer simulations. Icarus, 78, 411–425.

Zolotov, M.Y., 2012. Aqueous fluid composition in CI chondritic materials: Chemical equilibrium assessments in closed systems. Icarus 220, 713–729.